Revealing the transient formation dynamics and optoelectronic properties of 2D Ruddlesden-Popper phases on 3D perovskites

Tim Kodalle, Raphael F. Moral, Lucas Scalon, Rodrigo Szostak, Maged Abdelsamie, Paulo Ernesto Marchezi, Ana F. Nogueira, Carolin M. Sutter-Fella**

T. K., M. A, C. M. S.-F.
Molecular Foundry, Lawrence Berkeley National Laboratory, 1 Cyclotron Road, Berkeley 94710, USA
E-mail: csutterfella@lbl.gov

R. M., L. S., R. S., P. E. M., A. F. N
Institute of Chemistry, University of Campinas (UNICAMP), PO Box 6154, Cidade Universitaria Zeferino Vaz, Campinas, São Paulo 13083-970, Brazil
E-mail: anafla@unicamp.br

T. K. and R. M. contributed equally to this work.

Keywords: Two-dimensional metal halides, perovskites, in situ photoluminescence, formation dynamics, thin-film solar cells

Using in situ photoluminescence measurements during the spin-coating and annealing steps, we probed the formation of 2D layers on 3D triple cation perovskite films comparing phenylethylammonium and 2-thiophenemethylammonium iodide bulky cations. We elucidate the formation mechanisms of the surface layers for both cases and reveal two regimes during 2D layer formation: a kinetic-driven and a thermodynamic-driven process. These driving forces result in different compositions of the 2D/3D interface for each treatment; namely, different ratios of pure 2D (n = 1) and quasi-2D (n > 1) structures. We show that a higher ratio of quasi-2D phases is more beneficial for device performance, as pure-2D layers may hamper current extraction. Due to a more evenly distributed formation energy profile among 2D and quasi-2D phases, highly concentrated 2-thiophenemethylammonium iodide appears to be more suited for effective surface passivation than its phenylethylammonium analog.

1. Introduction

Perovskite solar cells (PSCs) have dominated photovoltaic (PV) research in recent years due to the fast increase in power conversion efficiency (*PCE*), now nearing 26%, and their ease of fabrication.[1] The enormous interest and excitement from the community brought this technology to a stage close to commercialization. However, the next major challenge for PSC technology, along with manufacturing upscaling,[2,3] is improving their long-term operational stability.[4] Various approaches have been engaged to improve their stability. For instance, perovskites are now often composed of a mixture of several cations and mixed halides,[5,6] leading to devices with higher *PCE*, better stability, and simplified preparation.[7,8] Recently, the use of bulky organic cations, generating 2D and *quasi*-2D perovskites with Ruddlesden-Popper (RP) and Dion-Jacobson (DJ) phases emerged to reduce non-radiative interface recombination and further improve the stability of 3D perovskite (3D-pvsk) thin films.[9–11]

Figure 1a(i) shows schematics of the crystal structure of a pure 3D-pvsk (ABX_3, where A is a monovalent cation, B is usually Pb^{2+} or Sn^{2+}, and X is a halide anion), as well as examples of 2D structures (**Figure 1a - ii** to **iv**). Conventionally, in a *true* 2D structure, the bulky cations (A') separate individual slabs of BX_6 octahedra; *i.e.*, the thinnest layer possible of the inorganic moiety (PEA_2PbI_4 and TMA_2PbI_4 in **Figure 1a - ii** and **iii**). In *quasi*-2D structures, the number of BX_6 inorganic slabs (n) is higher than 1, and an A-site cation from the ABX_3 perovskite is necessary to balance the charges of these structures (*e.g.*, $TMA_2[APbI_3]PbI_4$ in **Figure 1a - iv**). Therefore, if $n = \infty$ the material is precisely a 3D-pvsk and, for this reason, these 2D structures are commonly referred to as 2D-perovskites. The composition of the 2D perovskites can be generally described as $A'_2A_{n-1}B_nX_{3n+1}$ (RP-phase) or $A'A_{n-1}B_nX_{3n+1}$ (DJ-phase),[12] where A' is the bulky cation that forms the organic bilayer separating the inorganic slabs. The RP-phases are formed by monoammonium cations (*e.g.*, n-butylammonium) and the inorganic slabs are connected via Van der Waals interactions between their hydrocarbon backbone. In the case of DJ-phases, a diammonium cation (*e.g.*, 1,4-butanediammonium) is used instead, and the inorganic slabs are chemically connected to each other.[13] When incorporated in 2D/3D architectures, these bulky and hydrophobic cations (A' cations) are frequently deposited on already formed 3D-pvsk films and compete for the A-site,[14–17] but their large backbones separate the BX_6 octahedra layers into 2D structures.[18,19]

Despite the significant interest of the community in the application of bulky cations in PSCs, a clear understanding of the 2D phase and 2D/3D interface formation with dependence on the nature and concentration of the bulky molecule and its implication on the device performance

is still limited.[25–27] What makes these interfaces so complex and interesting is the variety of chemical compositions and properties of the bulky cations with different molecular backbones and functional groups that are readily available commercial chemicals.[28] This versatility, however, makes it difficult to draw general conclusions regarding the formation and functioning of the 2D/3D interfaces. Several properties of these bulky cations and their salts influence the 2D film formation, as well as incorporation into 2D/3D structures and, therefore, device performance: for instance, the length of the alkyl chain of the bulky molecule,[18,29,30] the choice of its halide anion,[16,31,32] and the choice of its aromatic backbones and their substituted analogues.[11,33–35] Furthermore, there is an ongoing debate about the optimal way of incorporating the bulky molecules into the 3D-pvsk film.[12] Depending on the choice of the molecule, and its exact deposition procedure the dimensionality of the 2D structure can be altered, which can affect the properties of the resulting devices.[31]

Some recent works have scrutinized the formation mechanisms of 2D perovskites with a variety of different bulky cations.[18,26,32–37] Liu et al.[26] treated the $FA_{1-x}MA_xPbI_3$ 3D-pvsk with neo-phenylammonium halide salts (neoPAX; X = Cl, Br, and I). They found that the choice of the halide can influence the type of RP-phase formed. The treatment with neoPACl, for instance, leads to the formation of both pure 2D and quasi-2D phases, while the Br, and I analogs only result in pure 2D phase. Conversely, the post-treatment of 3D-pvsk with linear alkylammonium cations always seems to form n > 1 RP-phases, and this seems to be independent of the alkylammonium chain length.[18,34,35] Additionally, Liu et al.[36] carried out a study with three different diamines: ortho-, meta-, and para-isomers of (phenylene)di(ethylammonium) iodide (x-PDEAI_2; x = ortho, meta, or para). They found that the only isomer capable of forming a n = 1 DJ-phase on the 3D-pvsk was the para-isomer, reflecting the strong steric hindrance of the ortho and meta counterparts. Another clear example of steric hindrance on the dynamics formation of 2D/3D perovskites is the work of Ghoreishi et al.[37] They modify $MAPbI_3$ perovskites with phenylethylammonium (PEA), benzylammonium (BZA), and anilinium iodide. The only difference between these three cations is the number of carbons they present in the alkylammonium chain attached to the aromatic ring, which affects the mobility and reactivity of these cations. As a result, PEA (2 carbons) forms 2D RP-phase with strong emission signature, BZA (1 carbon) forms RP-phases with poorer emission intensity, and no signal of phenylammonium (0 carbon) RP-phases could be found in both XRD and PL measurements. A constant observation regarding the PEA cation, whether explicit in the work or not, is that it tends to form mostly n = 1 RP-phases and, before thermal treatment, unreacted salt is detected by XRD.[12,15,34,37–39] However, modified PEA molecules such as 4-hydroxy-

phenylethylammonium and (3)4-fluoro-phenylethylammonium seem to change this tendency towards the formation of n ≥ 2 RP-phases.[34,35,40] In the work of Chen et al.,[35] the authors attribute this tendency of 3-fluoro-phenylethylammonium of forming n ≥ 2 RP-phases to a strain effect during the formation of the crystal. Finally, another class of commonly used bulky cation is the thiophene-derivatives such as 2-thiophenemethylammonium (TMA) and 2-thiopheneethylammonium (TEA). 3D-pvsk treated with TMA tends to form n = 1 and higher-order phases and, upon prolonged annealing, the n = 1 phase is converted to n ≥ 2, with n = 2 RP-phase being the most prominent.[15,41] This suggests that the n = 2 RP-phase for TMAI is the most thermodynamic stable phase. In the case of TEA, the post-treatment output is very similar to PEA: mostly n = 1 RP-phase is formed.[41] This similarity is apparently related to the number of carbon atoms between the thiophene ring and -NH_3+ (2 carbons) and steric hindrance effects, rather than the aromatic part of the molecule. All of the above described were carried out with post-treatment methods using bulky cation salt solutions in common perovskite anti-solvents such as isopropanol.

In the present work, we investigated the formation mechanisms of 2D RP-phases on 3D-pvsk thin films comparing two different bulky cations with iodide as counteranion, phenylethylammonium iodide (PEAI) and 2-thiophenemethylammonium iodide (TMAI, see Figure 1a). The cations used here contain one ammonium group, which promotes the formation of RP-phases. Using in-situ photoluminescence (PL) measurements during dynamic spin-coating and annealing of the 2D/3D-films, in combination with ex situ X-ray diffraction and photoluminescence excitation (PLE) measurements, we propose the formation pathways for the 2D RP-phases of each bulky cation and their influence on the optical properties of the 2D/3D-perovskite architectures. To obtain insights into the fundamental dynamics of these mechanisms, we vary the concentrations of the bulky cations and correlate our findings with the optoelectronic properties of corresponding solar cells. By elucidating the formation mechanisms of the 2D layers with a kinetic and thermodynamic regime during layer fabrication, different ratios of pure 2D (n = 1) and quasi-2D (n > 1) structures evolve for each treatment. Our results provide an understanding of the need to individually optimize the passivation strategy for each bulky molecule.

2. Results and Discussion

2.1. *In situ* PL during spin-coating and annealing

To gain information about the formation mechanisms of 2D RP-phases as passivants on 3D perovskite thin films, we employed *in situ* photoluminescence (PL) measurements. A PL excitation energy of 3.06 eV (405 nm) was used, and the measurements were performed during the formation of the 2D phase on the already formed 3D-pvsk. Two distinct bulky iodide cations, PEAI and TMAI, were deposited on top of triple cation $[(FAPbI_3)_{0.87}(MAPbBr_3)_{0.13}]_{0.92}(CsPbI_3)_{0.08}$ 3D-pvsk thin films. To do so, we spun the glass/3D-pvsk samples for 30 s at 4000 rpm in an N_2-filled glove box and dripped the respective bulky cation salts (1 - 80 mM dissolved in 2-propanol, IPA) after 7 s. After finishing the spin-coating step, we annealed the samples for 6 minutes at 100 °C. During both the spin coating and the annealing steps, we monitored the evolution of the PL signal (see Experimental Section for more details).

Figures 1b and **1d** show the resulting PL spectra for the cases of 80 mM TMAI and PEAI, respectively. The left panels show the spin-coating step; *i.e.*, time $t = 0$ s marks the beginning of the spin-coating process, and the black bars around $t = 7$ s indicate the dynamic dripping of the bulky molecules. The right panels in **Figures 1b** and **1d** show the PL evolution during the subsequent annealing step. Individual PL spectra of crucial points in time are shown in the Supplementary Information (SI) **Figure S1**. Before dropping the bulky cations, there is the expected PL-emission of the 3D-pvsk visible around $E_{3D} \approx 1.62$ eV in both cases. In the case of TMAI, this signal decreases and completely vanishes almost immediately after dropping the TMAI solution. At the same time, a second PL peak emerges at $E_{TMAI,1} \approx 2.37$ eV, which we attribute to the n = 1 2D RP-phase (see **Figure 1a**).[15] During the remainder of the spin-coating, no further evolution of the PL signal is observed. During the annealing step, the intensity of the n = 1 RP-phase gradually decreases, while the intensity of the 3D-pvsk gradually increases. Furthermore, almost immediately an additional peak appears around $E_{TMAI,2} \approx 2.20$ eV, which we attribute to the n = 2 RP-phase.[15] Interestingly, X-ray diffraction (XRD) patterns taken before and after the annealing step show not only the n = 1 peak but also the peak attributed to

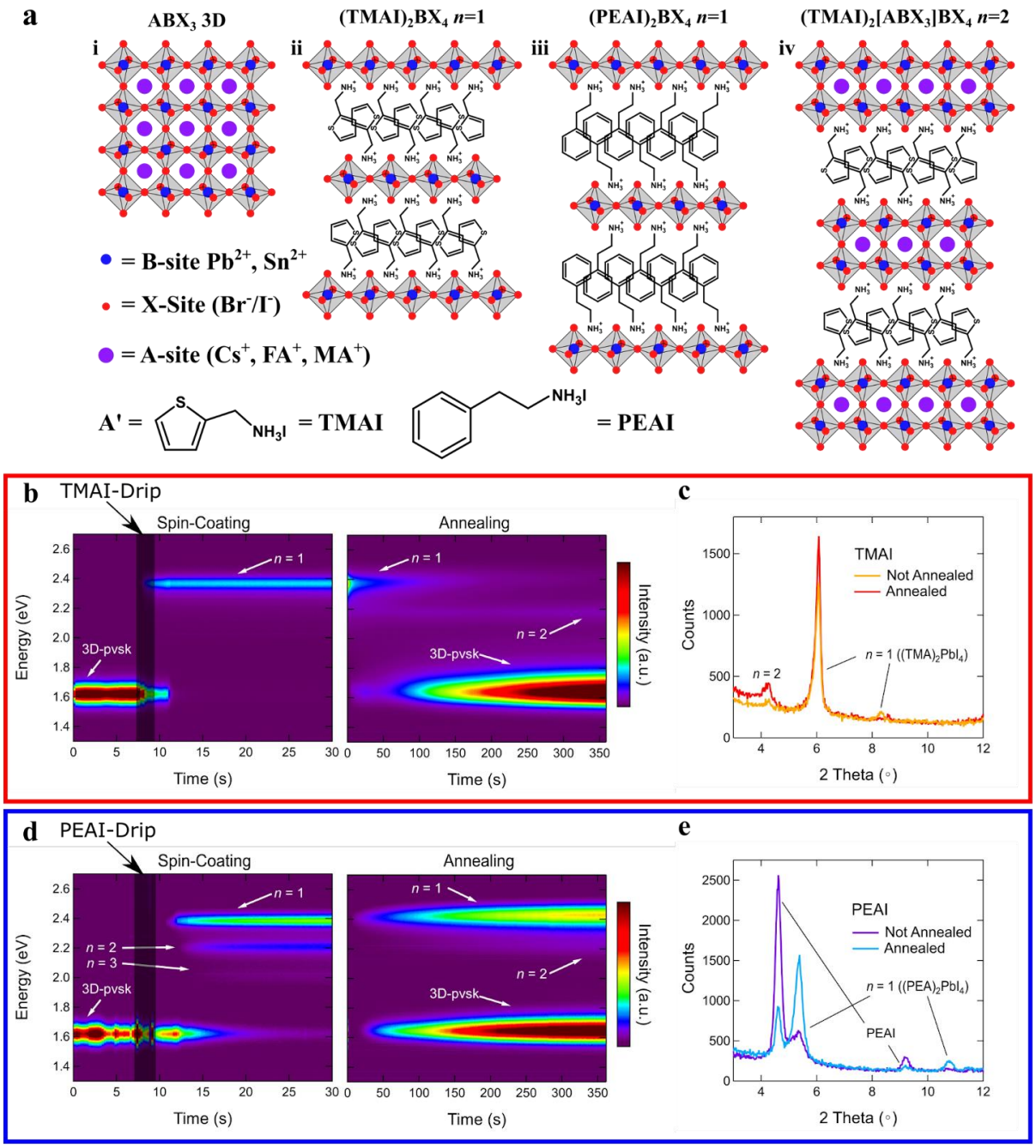

Figure 1: a) Left to right: Lattice structure of the 3D perovskite, *n* = 1 of TMAI and PEAI, and *n* = 2 of TMAI. Bottom left: Structural formulas of both molecules in their iodide salt. **b)** Contour plots of *in situ* PL measured during spin coating and subsequent annealing of TMAI (80 mM in IPA). **c)** XRD patterns of the respective films with TMAI after spin-coating and after annealing. **d)** and **e)** Corresponding PL evolution during spin-coating and annealing, as well as XRD measured after the respective steps in the case of PEAI (80 mM in IPA). In either case, the spin coating duration was 30 s at 4000 rpm with the dripping of the molecules after 7 seconds. Annealing was done at 100 °C for 6 minutes.

the n = 2 RP-phase (see **Figure 1c**).[42] Extending the PL measurements after the spin-coating; *i.e.*, mimicking the drying process that likely continues during the sample transfer from spin-coater to the XRD measurement (few minutes), we see that the n = 2 RP-phase forms rather quickly at room temperature, likely due to continued solvent evaporation (see **Figure S2** in the SI).

We interpret these results as follows: immediately after dropping the TMAI solution, the n = 1 RP-phase forms at the surface of the perovskite layer completely covering the 3D-pvsk film. We assume that the n = 1 layer is at least 50 nm thick and, therefore, absorbs the majority of the incoming photons due to the high absorption coefficient of metal halide perovskites of > 10^5 cm^{-1} above their bandgap energy.[43–45] Then, during annealing, the RP-layer (n = 1) intermixes with the underlying 3D-pvsk and thereby gets partly converted into the n = 2 RP-phase. Additionally, some TMAI molecules may diffuse into the perovskite film (*e.g.*, via the grain boundaries[22,46]) possibly reducing the absorption in the RP structure leading to increased excitation of the 3D-pvsk. The latter two processes might be accelerated and/or accompanied by a slight degradation of the RP-phases due to constant laser illumination at the elevated annealing temperature.

In the case of PEAI, the film evolution after dropping the molecules is retarded and more gradual (see **Figure 1d**). The 3D-pvsk peak gradually decreases in intensity without completely vanishing during the spin-coating. Interestingly, however, the PEAI dripping leads not only to the formation of the n = 1 RP-phase, but also to the formation of the n = 2 and n = 3 phases within less than 10 s after PEAI dripping during spin coating. It is interesting to note that we first observe the peak corresponding to the n = 1 RP-phase before the peaks corresponding to the n > 1 RP-phases appear. While this seems contradictory to a recent report from Sargent's group,[11] there are several differences in the experimental setup of both studies, which suggests that the formation dynamics of 2D RP-phases are strongly sensitive to the exact deposition parameters of the bulky molecule. During annealing, the 3D-pvsk emission behaves similarly as in the case of TMAI: with ongoing annealing time, the peak intensity increases. However, the n = 1 RP-related peak does not diminish as in the case of TMAI, but increases in intensity along with the n = 2 peak. Structural analysis was performed to find possible explanations for the different trends in the case of TMAI and PEAI (see **Figures 1c** and **1e**). By measuring XRD patterns of PEAI- and TMAI-treated films before and after annealing we find that, for PEAI, there is unreacted salt present on the surface of the 3D film,[12, 38] which is not the case for TMAI. During annealing, the intensity of the PEAI salt diffraction diminishes, while the intensity of the n = 1 ($(PEA)_2PbI_4$) diffraction increases, in agreement with the *in situ* PL measurements. This indicates that, for PEAI-treatment, the incorporation of the salt into the RP-phases is rather slow and still ongoing during annealing, while it is much faster and already completed during spin-coating in the case of TMAI. This may also be the reason for the stronger and more immediate suppression of the PL signal of the 3D-pvsk in the case of TMAI compared to PEAI. Additionally, it is interesting to note that in the case of PEAI, most of the RP-phase

forming during annealing is present in form of the n = 1 phase (compared to n > 1 RP-phases), while in case of TMAI the ratio of n = 1 to n = 2 RP-phases seems to decrease during annealing (see Figure 1 and **Figure S3**). In conclusion, using high concentrations of the bulky cation salts (80 mM), we see evidence that in the case of TMAI, an almost immediate reaction promotes the growth of a rather thick n = 1 RP-phase within < 2 s after dynamically dripping TMAI solution, completely suppressing the PL-emission of the 3D-pvsk. During annealing and following cool-down, this RP-phase intermixes with the 3D-pvsk forming n > 1 RP-phases and partly consuming the n = 1 phase. In the case of PEAI, we see a much slower and even incomplete conversion of the PEAI salt to the n = 1 RP-phase and direct conversion to n > 1 RP-phases during spin-coating, which seems to be partially reversed during annealing.

Before identifying possible mechanisms for this behavior, two additional effects should be discussed here. First, in both cases (TMAI and PEAI), the *in situ* PL measurements during annealing do not show contributions from n > 2 RP-phases. In the case of PEAI this seems surprising given the fact that we see n = 3 during spin-coating and, also in the case of TMAI, there is evidence of n > 2 phases after cool down of the sample after annealing (this will be shown in **Figure 3** and further discussed below). It is suggested that the PL signal is quenched at elevated sample temperatures,[47] and, therefore, likely suppresses the detection of the n > 2 phases, which show significantly lower intensity than n = 1 and n = 2 phases. Second, in the case of PEAI, there is no evidence of n > 1 RP-phases in XRD, although they are clearly detectable by PL, while we see a good agreement between XRD and PL in the case of TMAI. Here, we want to emphasize that the *in situ* PL provides information on radiative recombination processes and kinetics but does not provide structural or phase information. Also, photogenerated charge carriers can relax into lower energy states and, predominantly, emit from these states.[48,49]

To elucidate this further, we measured quantified steady-state PL (SSPL) of the 2D RP-phases synthesized separately via solution-process method (see the experimental section for synthesis details).[50] The SSPL shows a much higher PL quantum yield (PLQY) for the PEAI n = 1 phase compared to the TMAI n = 1 phase (see **Figure S4** and **S5** in the SI). Therefore, although the XRD patterns confirm the presence of n = 1 in both cases, a PL signal is detectable in the case of PEAI even at low amounts of *e.g.* $(PEA)_2PbI_4$ while larger quantities are needed in the case of TMAI-based RP-phases to show up in PL measurements.

To get more detailed mechanistic insights into the formation of the 2D RP-phases on 3D-pvsk and in particular for the different cases of PEAI and TMAI, we varied their concentration in IPA from 1 - 80 mM. **Figure S6** in the SI shows the evolution of the PL spectra measured

during spin-coating and annealing of 3D-pvsk films covered with 1, 4, 10, 40, and 80 mM. In the following, we will refer to these samples as TMAI-1, TMAI-4, …, TMAI-80 and PEAI-1, ..., PEAI-80. After subtracting a linear background from the spectra, we fitted each spectrum with a combination of one to four Gaussians (see **Figure S7** in the SI). The evolution of the respective fit parameters for all samples is shown in **Figures 2 and S8**. The left-hand side shows the PL parameters corresponding to the 3D-pvsk films and the right-hand side corresponding to the 2D, n = 1 RP-phase, respectively. Both are differentiated into spin-coating and annealing. The numberings (1)-(8) label trends described below.

First, we will focus on the evolution of the peaks corresponding to the 3D-pvsk (**Figures 2a** and **2c**), which are affected by the subsequent deposition of TMAI and PEAI in a very similar fashion. During spin coating of the bulky cations, the 3D-pvsk position remains unchanged indicating likely no strong interaction of the bulky molecules with the 3D-pvsk phase. In all ten samples, we see a PL position of $E_{3D} \approx (1.62 \pm 0.01)$ eV showing the high reproducibility of the 3D-pvsk process used in this study. During annealing, we observe a blue shift of all the peak positions of about 0.02 eV to 0.03 eV (Number (1) in **Figures 2a** and **2c**), which we attribute to temperature-induced bandgap-widening.[51] As for most of the samples, the PL-position stabilizes after about 10 s to 20s, which roughly coincides with the time it requires for the sample to reach the set temperature of 100 °C.

The intensity of the 3D-pvsk related peaks, in both cases, drops gradually after the deposition of the bulky cations (Number (2) in **Figures 2a** and **2c**). As expected, this effect is generally stronger pronounced in samples with higher molecule concentrations. For example, the intensity of the 3D-pvsk peak of TMAI-1 and PEAI-1 is only temporarily decreased during the dropping of the bulky molecules but remains unchanged otherwise. On the other hand, the intensity of the PEAI-80 sample, for example, drops gradually during the spin coating by more than 90% due to absorption by the evolving RP-phase. Additionally, for the same concentrations, this effect is more strongly pronounced in the case of TMAI compared to PEAI, which is in good agreement with the discussion above. For both TMAI-80 and TMAI-40, the intensity of the 3D-pvsk completely vanishes upon TMAI-dropping.

During the annealing, the PL-intensity decreases again during heat-up of the samples (first ~20 s, if not completely filtered by the RP-layer) due to thermal quenching (Number (3) in **Figures 2a** and **2c**). Here, it should be noted that the intensity is individually normalized for each panel in **Figure 2** and thus can only be compared with each other relatively. After the samples reach the final annealing temperature, the intensity increases (Number (4) in **Figures 2a** and **2c**),

which we attribute to a combination of several effects. First, an in-diffusion of bulky cations into the 3D-pvsk (*i.e.*, via grain boundaries),[22,46] mitigating the suppression of the excitation of the 3D-pvsk. Second, surface passivation due to the formation of the RP-phases, increasing the PLQY. Third, with increasing annealing time, the continuous laser illumination possibly first degrades the RP-phases and then the 3D-pvsk. Due to the latter effect, the intensity finally decreases - earlier for samples with lower concentrations of the respective RP-phase; *i.e.*, a thinner "protection layer" due to the laser degradation. A more detailed assessment of the role of the laser illumination can be found in the SI, **Figure S9**.

Next, we analyze the evolution of the RP-related peaks (**Figures 2b** and **2d**) during spin-coating and annealing. It is interesting to note that in the case of TMAI, the formation of RP-phases during spin-coating occurs for all concentrations > 4 mM but only at 80 mM for PEAI (see **Figures 1d** and **2d**). The position of the PL peak associated with the n = 1 PR-phase is constant during spin-coating and undergoes a blue shift during annealing (Number (5) in **Figs. 2b** and **2d**) in both cases. As this blue shift is much more gradual and slower than the one observed in the case of the 3D-pvsk (Number (1) in **Figures 2a** and **2c**), we do not attribute it dominantly to a temperature effect. Additionally, the PL peak position is observed at lower energies with higher concentration (Number (6) in **Figure 2b**), and its dependence on the concentration vanishes during the annealing-induced blue-shift (Number (5) in **Figures 2b** and **2d**) with the PL peak reaching a value of ~2.41 eV. To explain these trends in the PL peak position, we discuss a few possibilities below, and point out that they may occur concomitantly. In general, the bandgap of low-dimensional RP-phases is sensitive to BX_6 octahedral tilt, which is mostly controlled by the ion sizes and hydrogen bonding between the organic and halide ions.[52,53] These distortions change the amplitude of the Pb-I orbital overlapping and, therefore, affect the bandgap of the RP-phase.[52] Second, with the annealing, the preferential alignment of the organic cations' chain may change leading to a modification in crystal lattice and bandgap. Lastly, bromine diffusion from the surface of the 3D-pvsk into the n = 1 RP-phase would also increase its bandgap without significantly changing the bulk bandgap of 3D-pvsk, as observed in **Figure 2a**. This effect would be more pronounced in lower concentrations of TMAI treatment since the Br/I ratio would be higher at constant diffusion.

Focusing on the intensity of the n = 1 RP-phase now, it quickly increases and stabilizes after the dynamic deposition of the bulky cations (Number (7) in **Figs. 2b** and **2d**). During annealing, we see different behavior for TMAI and PEAI. In the case of TMAI, we see a gradual decrease of the intensity (Number (4) in **Figure 2b**) due to the same effects responsible for the increase of the intensity of the 3D-pvsk peak during annealing. In the case of PEAI, the evolution of the

intensity of the n = 1 RP-phase switches from monotonically increasing (PEAI-80 and PEAI-40) to a combination of initial in- and subsequent decrease (PEAI-10) with decreasing concentration (Numbers (4) and (8) in **Figure 2d**). Following the discussion above (**Figure 1d** and **1e**), we attribute the increase to the ongoing conversion of PEAI salt to the n = 1 RP-phase. In the case of PEAI-10, the salt is completely converted after 10 s, and subsequently the effects described under number (4) decrease the PL intensity.

In summary, we interpret the *in situ* PL and *ex situ* XRD data presented in **Figures 1** and **2** as follows. In the case of TMAI, the reaction from the TMAI salt to the n = 1 RP-phase seems to be very favorable (*i.e.*, have rather low activation energy) and spontaneously occurs even at room temperature during spin-coating for concentrations as low as 10 mM. Even for the highest concentration investigated here (80 mM), the salt is completely converted during the spin-coating process. However, there is no conversion from the n = 1 RP-phase to n > 1 phases during spin-coating but only during annealing. On the other hand, in the case of PEAI, the conversion of the PEAI salt to the n = 1 RP-phase seems to occur much slower: for concentrations below 80 mM we observe it only during heat treatment and, for concentrations above 10 mM, not all of the salt is converted to the n = 1 RP-phase. However, we observe the reaction between PEAI and the 3D-pvsk (forming n ≥ 1) at room temperature during the spin-coating only for PEAI-80, indicating a much slower formation and therefore different formation mechanism as in the case of TMAI. During annealing, we do not see direct evidence of a conversion of the n = 1 phase to n > 1 phases, as in the case of TMAI, but rather an accelerated conversion of the PEAI-salt to the n = 1 phase. It is noteworthy that, in the case of PEAI, the *in situ* PL is more sensitive than the XRD to detect the RP-phases, as mentioned before. Therefore, we assume that the detection limit of the PEAI-related RP-phases is rather low and that therefore its reaction on the 3D-pvsk film during spin coating occurs only very slowly in concentrations below 80 mM. The different reaction mechanisms for TMAI and PEAI with the 3D-pvsk film will be addressed further below.

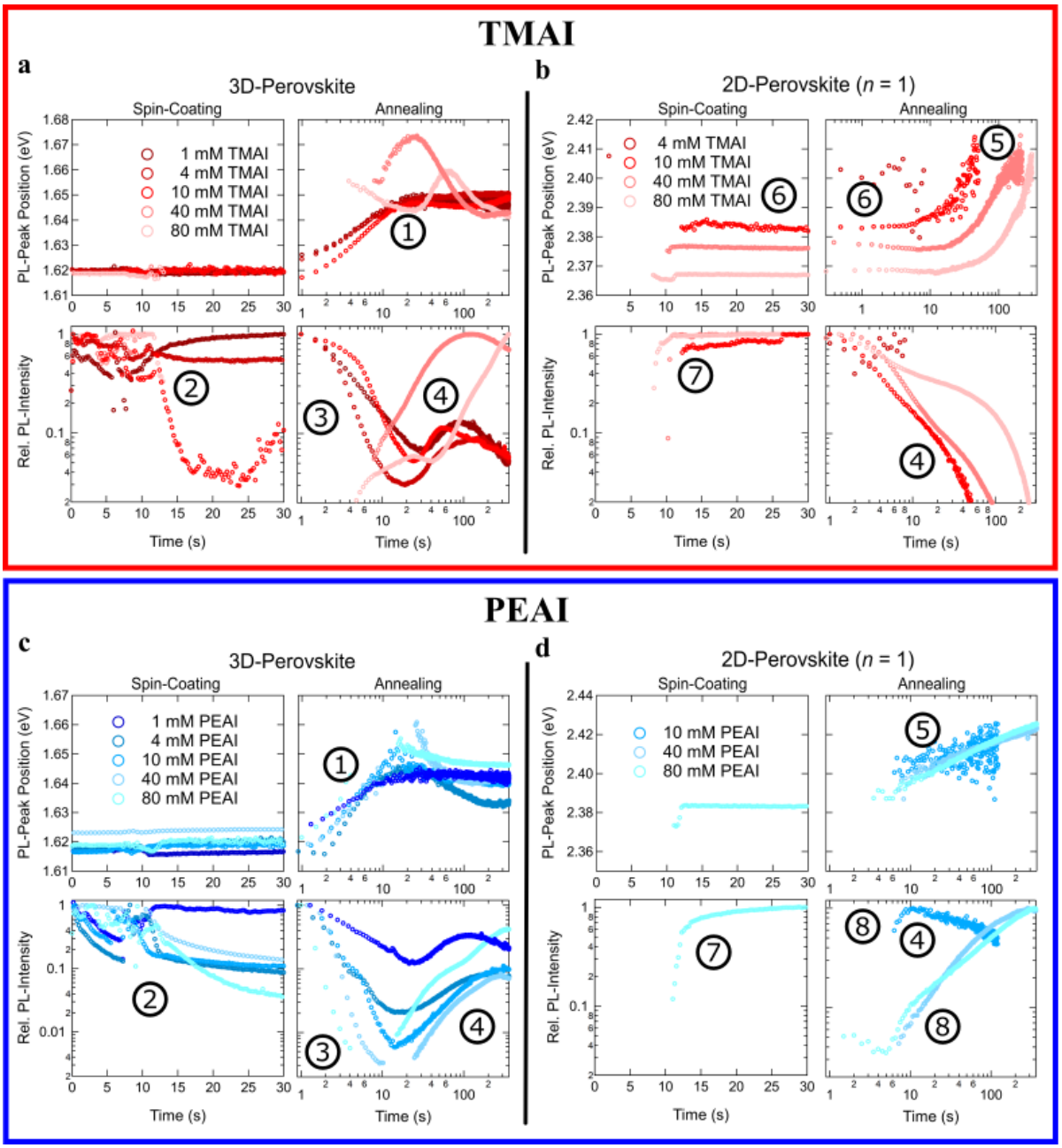

Figure 2. a) Evolution of the position (top row) and the intensity (bottom row) of the PL-peak corresponding to the 3D-pvsk, and **b)** evolution of the position (top row) and the intensity (bottom row) of the PL-peak corresponding to the n = 1 RP-phase during spin-coating and annealing of TMAI-treated 3D-pvsk films. **c)** and **d)** show the corresponding plots for PEAI-treated films. Note that not all samples show peaks related to the RP-phases (at all times) and they are consequently missing in some of these panels. Numbers (1)-(6) indicate trends described in the text.

To complement the picture of the RP-phase formation, we next analyze the 2D/3D stacks post-synthesis (after annealing) via *ex situ* XRD and SSPL. **Figures 3a** and **3b** show the diffractograms for both TMAI- and PEAI-treated samples with different concentrations after annealing. The corresponding patterns before annealing are shown in **Figure S10**. In both cases, as the concentration of the bulky cations increases, the intensity of the RP-phase diffractions increases proportionally, which is expected (note that the intensity scale is logarithmic). For

TMAI (**Figure 3a**) both n = 1 and n = 2 RP-phases are present (peaks marked with ***** for n=1 phase,[54] and peaks marked with **@** for n = 2 phase[42]), with no evidence of unreacted TMAI salt, even before annealing. This is in agreement with the SSPL profile which is composed of the emissions from the 3D-pvsk, n = 1, and n = 2 RP-phase (**Figure 3c**). For PEAI (**Figure 3b**) the XRD shows evidence of PEAI salt and n = 1 phase (peaks marked with **#** and with *****, respectively).[12,38] Again, SSPL confirms the presence of the 3D-pvsk (~1.6 eV) and n = 1 RP-phase (~2.4 eV) but the PEAI salt is not detected (**Figure 3d**). The peak positions marked with **&** and **$** (**Figure 3a** and **3b**) are the PbI_2 and 3D-pvsk diffractions, respectively. Since both bulky cations react with PbI_2, we observe a change in its diffraction intensity in both diffractograms. While for PEAI we see a monotonic decrease in PbI_2 peak intensity (**Figure 3b**), which is less apparent for TMAI (**Figure 3a**), it hints towards different reactivities of PEAI and TMAI with PbI_2.

Interestingly, for the TMAI-80 and TMAI-40 samples, there are PL emissions from n > 2 RP-phases (~1.8-2.2 eV, see **Figure 3c**). The appearance of these higher-order phases in SSPL (but not in diffraction) can be explained in terms of carrier funneling and energy transfer to lower energy states, which increase the emission intensity of the higher-order phases.[49] As already mentioned in the discussion of the *in situ* PL, it is noted that the ratio of n = 1 and n > 1 RP-phases depends on the concentration of the respective bulky molecule. This is very evident from the SSPL spectra of the TMAI samples, where the n > 1 RP-phases are dominant for low concentrations but, for the TMAI-80 sample, the dominating one is the n = 1 phase. In the case of PEAI, the trend appears to be more stable with n = 1 being the main phase for all concentrations > 4 mM.

To refine our analysis, particularly on charge carrier funneling, we measured the photoluminescence excitation (PLE) spectra of the PEAI-80 and TMAI-80 samples in different emission wavelengths. This type of measurement allows us to isolate the species on the surface responsible for a specific emission. A PLE spectrum, therefore, can be seen as an absorption spectrum resolved by the emission: we vary the excitation energy while measuring the PL intensity at a fixed emission energy (wavelength). Since the emission from the RP-phases and 3D-pvsk are far apart in terms of energy, we can clearly measure the PLE profile for each phase. To successfully isolate the PLE profile of each species, the spectra were measured at 540 nm or 530 nm (2.30 eV or 2.34 eV) for the n = 1 phase, 585 nm (2.12 eV) for the n = 2 phase, and at 800 nm (1.55 eV) for the 3D-pvsk (see the Experimental Section for further details).

The PLEs on the TMAI-80 sample are shown in **Figure 3e** with well-defined PLE spectra for both the n = 2 and n = 1 RP-phases with strong excitonic resonances (top and middle panels, respectively), in accordance with reported thin-film absorption spectra of similar materials.[44, 50] The strong excitonic resonance in the PLE of the n = 2 phase indicates a rather high amount of this material on the surface of the film, in agreement with our findings with SSPL (**Figure 3c**) and XRD (**Figure 2c**). Also, a little influence of the excitonic state of the n = 1 RP-phase (red arrow in the top panel) can be observed, indicating some level of carrier funneling from n = 1 to n = 2 RP-phase. Finally, a strong bleaching effect in the 3D-pvsk PLE is observed (bottom panel in **Figure 3e**), with two bleaching peaks in the same region of the excitonic resonances of the n = 1 and n = 2 RP-phases.

Following a similar analysis, **Figure 3f** shows the PLE spectra for all species present in the PEAI-80 sample. Only a discrete excitonic resonance close to 2.25 eV is observed in the PLE of the n = 2 phase (top panel in **Figure 3f**) and, in addition, it shows a strong contribution of the excitonic state of the n = 1 RP-phase (blue arrow). As in the case of TMAI, but much stronger, this is clear evidence of energy transfer (probably resonant)[55] between these two phases, where the n = 1 (higher bandgap) transfers energy to the n = 2 (lower bandgap) RP-phase. This helps explain why we observe the n = 2 phase in the *in situ* PL during the spin-coating but do not observe it in the XRD. Therefore, in agreement with our previous discussion, the n = 1 RP-phase is dominant in the case of PEAI, and the n = 2 RP-phase might be present only in small domains. Regarding the PLE at the n = 1 RP-phase emission, as expected, we see a well-resolved PLE profile with a strong excitonic resonance with a maximum at 2.48 eV (middle panel in **Figure 3f**). Also, in the PLE from the 3D-pvsk (bottom panel), a strong bleach in the spectrum is observed right at the excitonic absorption of the n = 1 RP-phase (~2.48 eV), which shows a similar filter effect as observed in the case of TMAI. It is noteworthy that, although this filter effect is significant, the PLE intensity of the 3D-pvsk does not completely vanish in energies ≤ 2.48 eV *(i.e.*, the n = 1 RP-phase absorption region).

Finally, **Figure 3g** shows a comparison between all the PLEs from the 3D-pvsk on the PEAI-80, TMAI-80, and not-treated perovskite film. It is clear that there is no energy transfer from the RP-phases to the 3D-pvsk, since we observe bleach peaks instead of positive peaks in the absorption window of the RP-phases (*i.e.*, ≤ 2.20 eV). In other words, if energy transfer occurred, the PLE spectra of the 3D-pvsk in this window should show an increase in intensity, like the one we see in the PLE spectrum of the n = 2 RP-phase in PEAI-80 sample (top panel in **Figure 3f**). It does not mean, however, that energy/charge transfer does not occur in these

systems under bias voltage, for example, in a solar cell device. A final remark on this comparison is that the bleaching effect of TMAI is much stronger than it is for PEAI samples; this finding is in close agreement with our *in situ* PL analysis during spin-coating (Number (2) in **Figures 2a** and **2c**), where the intensity of 3D-pvsk emission vanishes upon addition of TMAI solution, but the same does not happen with the addition of PEAI solution.

Lastly, we collected scanning electron microscopy (SEM) images (**Figure S11a**) of three representative concentrations of PEAI and TMAI solutions. For PEAI samples, we see a gradual and homogeneous coverage of the films through all conditions, and the 2D layers are visible for concentrations ≥ 10 mM, in agreement with the SSPL and XRD from **Figure 3**. In the case of TMAI, we see a smooth coverage of the films for all the concentrations up to 40 mM. In the TMAI-80 sample, a significant morphological change occurs, and flake-like structures are formed on the surface of the film. Likewise, its PEAI analogue, the TMAI samples also show the PL emission and XRD diffraction characteristics of the RP-phases in samples prepared with concentrations ≥ 10 mM. Therefore, we conclude that a threshold concentration of the bulky cation solutions for RP-phase formation seems to lie between 4 and 10 mM. Also, in this low-concentration regime, atomic force microscopy (AFM) measurements revealed a decreased root mean square roughness (S_q) when compared to the control sample (see **Figure S11b**), which can benefit the interlayer contact between adjacent layers in a solar cell, for instance. The TMAI-treatment seems to impact more directly the square roughness compared to PEAI, which can be explained by the thicker layers and consequent change of morphology caused by the RP-phases formed in TMAI samples.

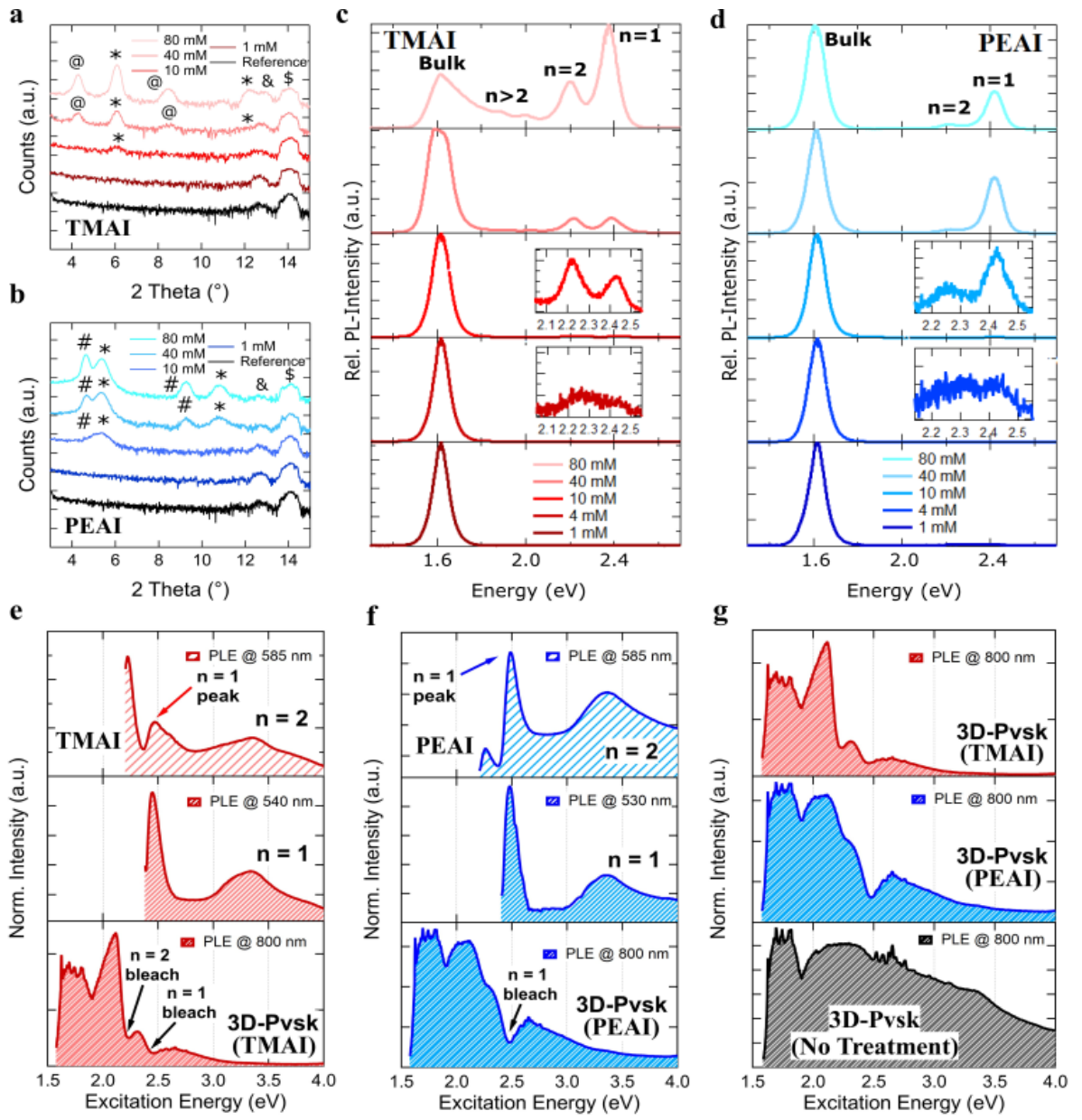

Figure 3: XRD patterns for the modified 3D-pvsk films with various concentrations of the treatment solutions of the bulky cations **a)** TMAI and **b)** PEAI. *, @, &, #, and $ indicate n=1 phase, n=2 phase, PbI_2, PEAI salt, and 3D-pvk diffraction, respectively. **c)** Steady state PL of samples with varied concentration of TMAI. **d)** Steady state PL of samples with varied concentration of PEAI. **e)** PLE spectra measured at different emission maxima on the TMAI-80 sample. **f)** Same as in **e** but with the PEAI-80 sample. **g)** Comparison between the PLEs at the 3D-pvsk emission (800 nm) with and without treatment with bulky cations. All data shown in this figure was taken after annealing of the 2D/3D films.

2.2. Reaction Dynamics and Energy Diagrams

To provide some mechanistic understanding of the transient formation dynamics of 2D RP-phases, kinetic and thermodynamic considerations are discussed in the following paragraphs. In kinetically driven chemical reactions, the products are formed according to their relative rates of formation (rate-limiting-step); in the thermodynamic reactions, the products are formed

according to their equilibrium of interconversion and/or conversion of intermediates, formed during the rate-limiting-step, to their equilibrium products.[56–58] In our experiments the spin-coating is the rate-limiting-step and the annealing is the thermodynamic step.

We propose a qualitative energy diagram (**Figure 4**) of the reactions occuring during spin-coating and annealing considering two initial conditions: (i) salt (PEAI or TMAI) + 3D-pvsk and (ii) salt + PbI_2. Given the available precursors, the products of the first initial condition (salt + 3D-pvsk) may include n = 1 and higher RP-phases, while only the n = 1 RP-phase can form following the second condition (salt + PbI_2). The activation energy for the reactions are labeled $E_{\mathbf{P}}$ for PEAI and $E_{\mathbf{T}}$ for TMAI.

During spin-coating of the PEAI samples, we observe the formation of the RP-phases from n = 1 to n = 3 while some unreacted salt remains at the surface. The latter indicates that the activation energy for the reaction of PEAI + PbI_2 (E_{P1} - **Figure 4a**) is higher than k_BT and, therefore, does not occur during spin-coating. The formation of the RP-phases up to n = 3 (**Figure 1d**), however, shows that the PEAI is partially reacting with the 3D-pvsk, suggesting that $E_{P2} \gtrsim k_BT$. E_{P2} being slightly higher than k_BT is consistent with the fact that we only observe the formation of RP-phases for PEAI-80 samples during spin-coating but not for lower concentrations. We assume that the reason for this concentration dependence is that only molecules with rather high energy at room temperature (*i.e.*, outliers in the kinetic energy distribution, compared to the median) have enough energy to react. As the absolute number of outliers increases with concentration, we are able to detect the reaction at high concentration.

The energy profile is quite different for TMAI. During spin-coating, a prompt formation of the n = 1 RP-phase is apparent by *in situ* PL, and no unreacted salt is detected by the XRD after spin-coating. The fact that the salt is completely converted to only the n = 1 RP-phase indicates a fast reaction between TMAI and PbI_2, suggesting that $E_{T1} < k_BT$ (**Figure 4b**). However, small amounts of n = 2 RP-phase also form during the drying process after spin-coating, which indicates that E_{T2} (TMAI + 3D-pvsk) is equal or slightly lower than k_BT ($E_{T2} \lesssim k_BT$).

After the spin-coating step (rate-limited-step) is complete, we have a mixture of different products with different local minima that depend on their individual formation energy. Once heat is supplied to the system during the annealing step, further reactions between unreacted precursors (PEAI case) and kinetic products to thermodynamic products take place. The final composition of the materials, therefore, will depend on the relative depth of the formation

energy of each different RP-phase. Our experiments suggest that the energy profile for PEAI is quite uneven; namely, the formation energy for the n = 1 RP-phase is much lower than the higher order phases with n > 1, as represented in the energy diagram of **Figure 4a**. As supported by previous density functional theory (DFT) calculations, the formation of n = 1 RP-phase for PEAI is favored due to its large negative formation energy compared to the n = 2 and higher phases; this is related to the increased van-der-Waals interaction between the organic molecules in the organic bilayer.[59,60] As such, during annealing, both the unreacted salt and higher order phases tend to convert to the n = 1 phase, resulting in a final film composition that is mainly composed of $(PEA)_2PbI_4$ and the 3D-pvsk. Only a relatively small signal of the n = 2 phase is found in the SSPL after annealing (**Figure 3d** - top), and absolutely no evidence of this phase is found in the XRD (**Figure 3b** - top).

Regarding the TMAI treatment, the resulting energy profile is more even with close energy minima for all RP-phases. In fact, previous reports suggest that the n = 2 RP-phase is thermodynamically more stable than the n = 1 RP-phase for TMAI, which is in good agreement with the results of our prolonged annealing experiment (see **Figure S3**).[15,41] This trend is also observed in analogue butylammonium-based RP-phases: the formation energy of the lower family members (*i.e.*, n = 1 to n = 3) have similar, negative formation energies, with the n = 2 presenting the lowest among them.[57] This similarity makes it difficult to achieve pure-phase materials during the synthesis with butylammonium, which seems to be the case for TMAI as well. As discussed above, during spin-coating mostly the n = 1 phase is formed due to the lower activation energy for the reaction between TMAI and the readily available PbI_2 (E_{T1}). After annealing, however, a mixture of several phases can be observed in the final composition of the film, showing evidence of even n = 3 and n = 4 RP-phases for high concentrations (**Figure 3c** - top). Furthermore, the corresponding XRD patterns (**Figure 1c** and **Figure 3a**) show an increase in the intensity of the diffraction peaks related to the n = 2 RP-phase after annealing. This heterogeneous composition suggests that the formation energy of these RP-phases is very similar, with the n = 2 being possibly the most stable. Thus, the whole dynamics of the TMAI treatment can be summarized in the energy diagram of **Figure 4b**. Further discussion and details regarding this energy diagram can be found in the **Supplementary Text 1**.

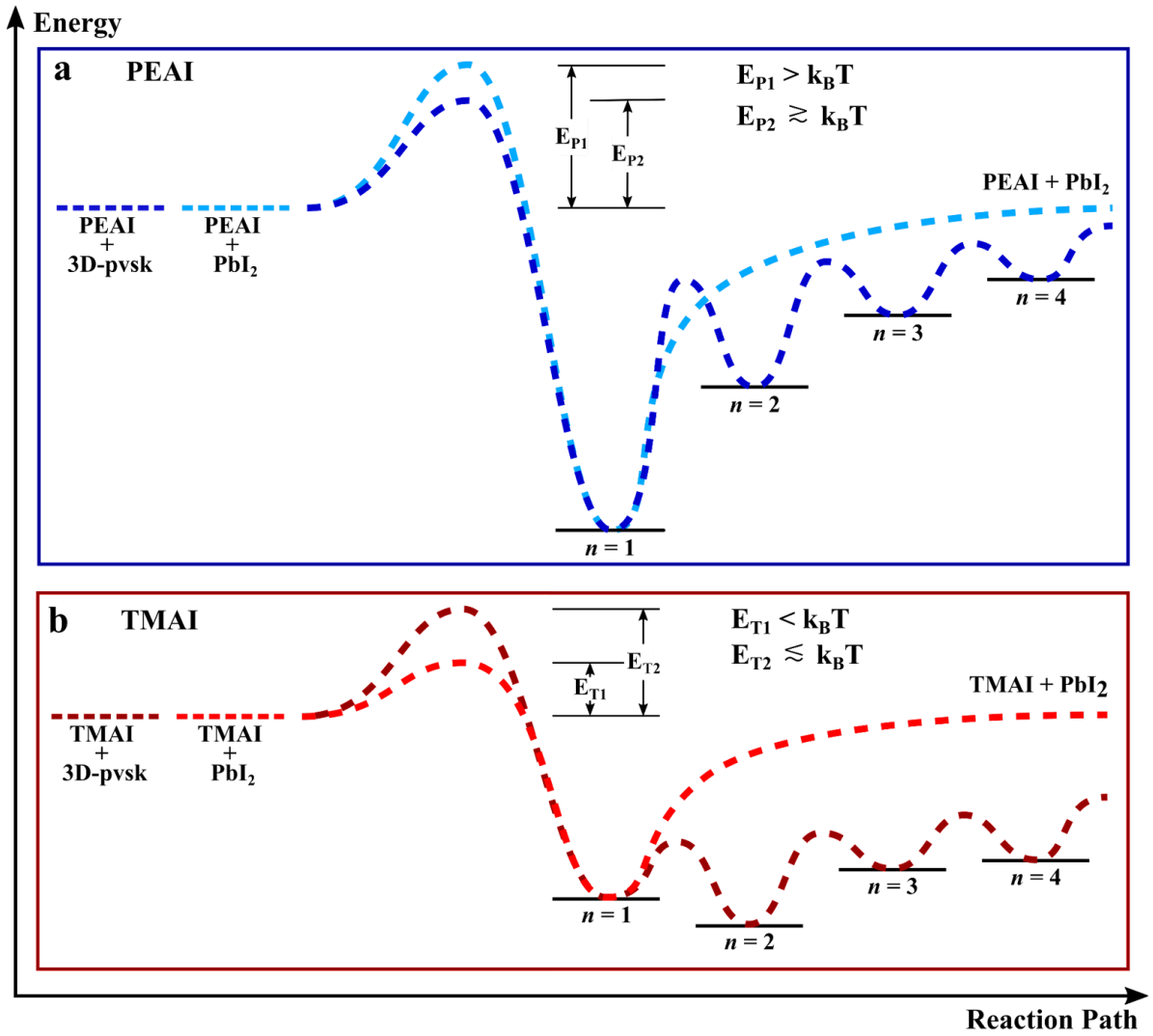

Figure 4: Qualitative energy diagrams for the reactions of **a)** PEAI and **b)** TMAI with the 3D-pvsk films considering two different reaction substrates: PbI_2 and 3D bulk perovskite.

2.3 Device Performance

Finally, to close the loop between *in situ* observations, and the proposed interplay between kinetics and thermodynamics, we assembled *nip*-type perovskite solar cells (PSC) with the architecture FTO/SnO_2/3D-pvsk/RP-phases/Spiro-OMeTAD/Au. It is worth pointing out that, for all the samples in this experiment, we performed thermal annealing after the deposition of the bulky cation, following the same procedure as during the *in situ* PL experiments.

Boxplots of all solar cell parameters are shown in **Figures 5 and S12**. They show that both salts can improve the *PCE* of the corresponding devices; however, the maximum of the *PCE* is reached at a much lower concentration in the case of PEAI (4 mM) than in the case of TMAI

(40 mM). To understand this trend, we analyze each photovoltaic parameter individually, connecting them to the mechanistic insights discussed above.

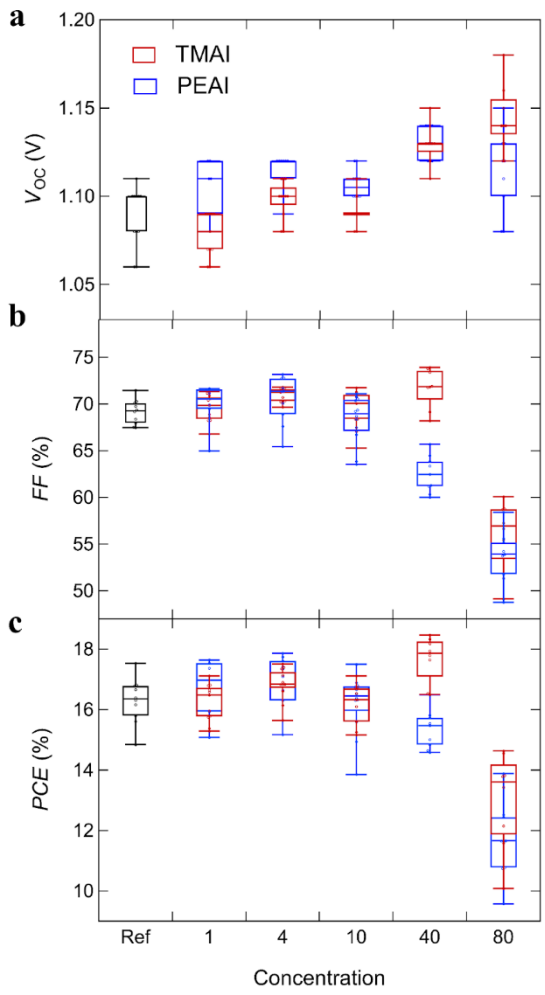

Figure 5. Boxplots of the V_{OC} (a), *FF* (b), and *PCE* (c) of solar cell devices treated with varied concentrations of PEAI or TMAI. Here shown are the reverse measurements, see **Figure S12** for a more detailed representation of the PV parameters.

Up to concentrations of 10 mM, the open-circuit voltage (V_{OC}) is constant for TMAI and slightly improving for PEAI. For concentrations ≥ 40 mM, there is an (additional) increase of V_{OC} for both bulky molecules, with the highest median for TMAI-80 and PEAI-40. The fill factor (*FF*) has the most dominant influence on *PCE*; *i.e.*, shows very similar trends: for low concentrations, *FF* is steadily increasing up to a maximum from which it quickly deteriorates with higher concentrations. This maximum is at 4 mM for PEAI and 40 mM for TMAI.

Both the trends of fill factor (*FF*) and open circuit voltage (V_{OC}) can be explained by the formation mechanics unraveled by *in situ* and *ex situ* characterization above. Due to the differences in the energy profile of PEAI and TMAI (**Figure 4**), the final mixture of 2D and *quasi*-2D layers (*i.e.*, the ratio of n = 1 to n > 1 RP-phases) is different for each molecule. In

the case of PEAI, most of the reacted salt is present in form of the n = 1 RP-phase (see **Figure 3d**), especially for concentrations above 4 mM. Additionally, there is unreacted salt present at the surface of the film even after annealing of the PEAI-40 and PEAI-80 samples. In the case of TMAI, on the other hand, most of the reacted salt forms n = 2 and higher RP-phases with the exception of TMAI-80 (see **Figure 3c**).

Interestingly, for both molecules, *FF* drops at the concentration at which the n = 1 phase becomes dominant compared to n > 1 RP-phases (*i.e.*, at PEAI-10 and TMAI-80, compare **Figures S12** and **3c** and **d**). On the other hand, only samples showing a significant amount of the n = 1 RP-phase, lead to improved V_{OC}. We, therefore, propose the following integrated mechanism. The pure 2D phase (n = 1) provides better passivation of surface defects via reduction of nonradiative recombination,[61] increasing V_{OC} and subsequently *FF*.[62] This is in good agreement with recent reports for inverted PSCs.[35,63] However, the insulating character of the n = 1 phase ([12]) leads to a barrier for the current extraction reducing *FF* if present in large amounts; *i.e.*, higher concentrations of the salt leads to thicker insulating interface layers and, therefore, a more effective current barrier. Similar barriers for photocurrent extraction due to surface treatments have been proven for inorganic chalcopyrite thin-film solar cells and a direct correlation between the thickness of a resistive surface layer and a detrimental effect on *FF* was shown.[64,65] In the case of PEAI-40 and PEAI-80, the current barrier might be amplified by the unreacted salt present at the surface.

The n > 1 RP-phases, on the other hand, are not as detrimental for the *FF* but also do not passivate the surface defects as effectively. As discussed above, the formation of n > 1 RP-phases requires the incorporation of organic cations from the 3D-pvsk, thereby facilitating an intermixing of the 2D and 3D phases. In contrast, the n = 1 phases may be formed by reactions of the salt and the excess PbI_2 on the surface, consequently lacking intermixing with the 3D-pvsk. Considering that the quantum and dielectric confinement of the charge carriers is higher in n = 1 RP-phases compared to the n > 1,[66,67] and assuming charge and/or energy transfer from 3D to 2D phases,[57] we can conclude that the charge carriers in the n = 1 phases are more difficult to be separated. Consequently, we assume a higher electric resistivity and, therefore, poorer transport properties in the case of n = 1 RP-phases than in the case of n > 1 phases, which helps explain the *FF* trends.

Taken together, there is a trade-off of a beneficial passivation effect (increasing V_{OC} and *FF*) and a detrimental barrier effect (reducing *FF*) – depending on the amount of n = 1 and n > 1

RP-phases. The fact that the formation of the n = 1 RP-phase can be detrimental to the device's performance is in agreement with recent reports that the formation of PEA_2PbI_4 hinders the charge transport, reducing *FF* and the overall performance.[12,61] It might also explain why some groups achieve the highest *PCE*s using PEAI-treatment without any thermal annealing,[12,68,69] as this procedure might "freeze" the kinetic products (*i.e.*, result in rather low amounts of the n = 1 RP-phase).

The short-circuit current density (J_{SC}) stays constant without any clear trend for both salts, and only decreases drastically at 80 mM. We attribute this abrupt drop at PEAI-80 and TMAI-80 to the formation of large platelets of RP-phases resulting in a very rough morphology as observed in the SEM and AFM images (see **Figure S11**).

3. Summary and Outlook

In summary, we compared the formation dynamics of two different 2D RP-phases, TMAI and PEAI, using a combination of *in situ* PL as well as *ex situ* material and device characterization. We found that in the case of TMAI, the conversion from the bulky molecule to the n = 1 RP-phase occurs very fast and that during annealing a further conversion to higher-order phases takes place. In the case of PEAI, on the other hand, the conversion is slower (and even incomplete for high concentrations). Additionally, we find that, for PEAI, the annealing rather leads to a conversion to the thermodynamically most stable n = 1 RP-phase than to higher-order phases. Thiophene alkylammonium salts seem to be promising candidates for optimization, due to their even energy profile enabling the targeted formation of mixtures of n =1 and n > 1 RP-phases, making it a rather robust surface treatment. Due to these different formation dynamics, the interface properties of the 2D/3D perovskites depend strongly on the bulky molecule used, its concentration and consecutive heat treatment after spin coating. Subsequently, a careful, and individually tailored optimization of the deposition parameters are needed for each bulky molecule. These mechanistic insights also explain why recent studies found that un-annealed PEAI leads to higher *PCE* than annealed PEAI. Due to the insulating character of the n = 1 RP-phase and the pristine salts, we achieve better passivation effects using higher concentrations of TMAI than PEAI, making it a very promising molecule for high-efficiency devices. This study illustrates how mechanistic insights unveiling thermodynamic and kinetic contributions can guide the fine-tuning of 2D/3D architectures avoiding an Edisonian trial and error approach.

4. Experimental Section

Preparation of the 3D-perovskite thin films for materials characterization: The triple cation $[(FAPbI_3)_{0.87}(MAPbBr_3)_{0.13}]_{0.92}(CsPbI_3)_{0.08}$ perovskite thin films were deposited in a N_2-filled glovebox from a solution containing FAI (GreatCell Solar Materials), MABr (GreatCell Solar Materials), PbI_2 (TCI America), $PbBr_2$ (TCI America), and CsI (Sigma-Aldrich) with a concentration of 1.3 M. We used a slightly Pb-rich composition (Pb:(FA,MA,Cs) = 1.05:1.00). The precursor was dissolved in a mixture of anhydrous N, N-dimethylformamide (DMF, Sigma-Aldrich), and dimethyl sulfoxide (DMSO, Sigma-Aldrich) with a volume ratio of DMF:DMSO = 4:1 at room temperature. The 3D perovskite films were spin-coated using a one-step process, where 50 µl of the precursor solution was deposited on a 1.7x1.7 cm^2 sized glass substrate before starting the spin-coating process. Spin-coating was performed at a speed of 2000 rpm for 12 s followed by 5000 rpm for 30 s. 15 s before the end of the spin-coating, 150 µl of chlorobenzene were dropped on the spinning film. Subsequently, the samples were annealed for 60 minutes at 100 °C. The glass substrates were cleaned with soapy water, acetone, and isopropanol, and then plasma-treated for 5 min right before perovskite deposition.

***Preparation of the polycrystalline RP-phase for materials characterization*:**

for n = 1 RP-phases: 96 mg of PbI_2 (0.21 mmol) was dispersed in 5 mL of toluene and 1 mL of butyric acid. This dispersion was placed under magnetic stirring, and 0.5 mL of the amine (phenylethylamine or 2-thiophenemethylamine) was added to it. The flask was, then, allowed to stir at room-temperature for about 3 minutes. After this time, the $(PEA)_2PbI_4$ is formed (green luminescence under UV light) in the reaction with phenylethylamine, and a clear yellow solution is formed with 2-thiophenemethylamine. The later, upon gentle heat (*ca*. 60 °C), a slow precipitation of the $(TMA)_2PbI_4$ occurs. The solid material is, then, separated by centrifugation (6000 rpm for 5 min.), washed with neat toluene (5 mL), and centrifuged again in the same conditions. The toluene is discarded, and the yellow solid is dried under N_2 flow. This solid was used to perform the SSPL measurements in Figure S5.

for n > 1 RP-phases: a separate formamidinium acetate [FA(OAc)] solution is prepared by dissolving 23 mg (0.22 mmol) of FAOac in 3 mL of toluene and 1 mL of butyric acid. This solution was transferred to a syringe and promptly injected into the reaction mixture obtained before the first centrifuge step of the above procedure (n = 1 RP-phase synthesis). In the case of $(PEA)_2PbI_4$, nothing occurs at first and, upon heating the mixture at 80 °C for a few minutes, the yellow powder slowly turns into a vibrant red color. In the case of $(TMA)_2PbI_4$, a rapid reaction took place upon injection of FAOAc solution, forming a dark-red/brown solid; upon heating at 80 °C for a few minutes, the product turned into a more vivid red color indicating the formation of n > 1 RP-phases (mostly n = 2 in both cases). The solids were separated *via* centrifugation as well (6000 rpm for 5 min.) and washed once with neat toluene. These solids were used for the XRD measurements.

Synthesis of the ammonium salts

Synthesis of phenylethylammonium iodide (PEAI): Synthesis of phenyl ethyl ammonium iodide (PEAI): to a 50 mL round bottom flask equipped with a magnetic stir bar, 6 mL of isopropanol, and 1.04 mL (1 g, 8.25 mmol, 1 eq.) of phenylethylamine was added. The solution was stirred at 0 °C in an ice bath for 15 min and then 1.42 mL (1.34 g, 10.75 mmol, 1.3 eq.) of HI 57 wt% was added dropwise for 15 min. The reaction proceeded for 3 h, and it was gradually cooled to room temperature. In sequence, the solvent was evaporated under reduced pressure. The solid obtained was poured into the toluene (5 mL) and stirred under heating (80 °C) for ~20 min. After reaching room temperature, diethyl ether was added and the solid was filtered. Following this, the product was recrystallized three times using absolute ethanol and diethyl ether. Finally,

the white solid was dried in a vacuum oven at 80 °C for 8 h and transferred to an N_2-filled glove box.

Synthesis of 2-thiophenemethylammonium iodide (TMAI): to the synthesis of TMAI, we used the same protocol described for PEAI, only changing phenylethylamine by 2-thiophenmethylamine.

The PEAI and TMAI powders were then dissolved in IPA (varying from 1 mM to 80 mM concentration) and dynamically deposited onto the 3D perovskite films. Thereby, the spin-coating was performed at 4000 rpm for 30 s. The salt solution was dripped at 7 s after starting the spin-coating. Afterward, the films were annealed at 100 ℃ for 6 minutes.

Preparation of solar cells: The FTO-coated glasses were cleaned by an ultrasonic bath in Hellmanex solution 2% in water (15 min), acetone (15 min) and isopropanol (15 min). The substrates were dried with compressed nitrogen. They were thereafter treated in UV-ozone cleaner for 20 min. A SnO2 layer was deposited by 3.75% SnO_2 nanoparticle (SnO_2, 15% in H_2O colloidal dispersion, Alfa Aesar) in water at 4000 rpm for 30 s, and annealed in ambient air at 150°C for 30 minutes. Before perovskite deposition, the substrates were treated with UV-ozone for 20 minutes and then transferred to the glovebox filled with nitrogen for perovskite deposition. The perovskite deposition was carried out similar to that described previously. The hole transport layer was prepared by dissolution of 2,2',7,7'-tetrakis(N,N'-dip-methoxyphenyl-amine)-9,9'-spirobifluorene (Spiro-OMeTAD), lithium bis(tri-fluoromethanesulfonyl)imide (Li-TFSI, 1.8 M in acetonitrile), tert-butylpyridine (tBP) and tris(2-(1H-pyrazol-1-yl)-4-tert-butylpyridine) cobalt(III) tri[bis(trifluoromethane)sulfonimide] (FK209, 0.25 M in acetonitrile) in the proportion 1:3.3:0.5:0.05 in chlorobenzene. The HTM solution was spin-coated dynamically on a rotating substrate at 4000 rpm. An70 nm-thick gold top electrode was deposited as a top contact electrode by thermal evaporation under high vacuum.

Solar cell characterization: The *J-V* characteristic of the solar cells were obtained using a Keithley 2400 Source Meter under simulated one-sun AM 1.5G illumination (100 $mW.cm^{-2}$) with a solar simulator (Asahi, HAL-320). The light intensity was calibrated before each *JV* scan using a silicon pin photodiode previously calibrated by a KG5 filtered silicon reference cell. The devices were measured both in reverse scan (1.2V to 0V) and forward scan (0 V to 1.2 V) with steps of 0.01 V and a delay time of 100 ms. The cells were masked with a black metal mask limiting the active area to 0.16 cm2 and reducing the influence of the scattered light.

In situ photoluminescence measurements: The *in situ* PL measurements were carried out using a home-built setup in an N_2-filled glove box. Excitation was performed using a laser diode emitting at 405 nm and the PL emission was collected using an optical fiber coupled with an Ocean Optics spectrometer ("Flame") calibrated by the manufacturer. We applied a Jacobian correction to the data transforming them from wavelength- to energy-space and removed a linear background before fitting them using a combination of one to four Gaussians depending on the presence of RP-phases. We used integration times of 250 ms during spin-coating and 500 ms during annealing. The spectra shown in Figure 3 were recorded with the same setup using integration times of 2 s. The *in situ* measurements were performed at least four times with each composition to verify that the described trends are reproducible.

Scanning electron microscopy: SEM images were collected using a FEI Quanta FEG 250 and an electron beam acceleration of 10 kV.

X-ray Diffraction: The XRD patterns were taken with a Rigaku SmartLab X-ray diffractometer using Cu Kα radiation.

Photoluminescence Excitation Spectra (PLE): all the spectra were collected in a Horiba-JOBIN YVON Fluorolog-3 with a xenon lamp as the excitation source. For the PLE at 800 nm (3D-pvsk), the film was placed at 45 ° with respect to the excitation and the detection was collected from the back-face of the substrate (glass side - film at 135 ° with respect to the detection axis), so that we could verify the influence of all the species on the surface of the 3D-pvsk on its PLE profile. For the PLEs of the RP-phases, the spectra were collected in front-face position (at 45 ° with respect to the excitation axis and 45 ° with respect to the detection axis) to be able to resolve the PLE profile of the RP-phases. The emission wavelength for each species was different: 800 nm for 3D-pvsk; 530 and 540 nm for n = 1 RP-phase of PEAI and TMAI, respectively; and 585 nm for the n = 2 RP-phases. The excitation window was always from 300 nm to 15 nm before the emission wavelength (to avoid strong scattering artifacts). The integration time at each wavelength was 0.6 s and the step was 1 nm at a time.

Supporting Information

Supporting Information is available from the Wiley Online Library or from the author.

Acknowledgements

T.K. and R.F.M. contributed equally to this work.

T.K. thanks the German Research Foundation (DFG) for funding (fellowship number KO6414). R.F.M. acknowledges the support from the São Paulo Research Foundation (FAPESP) — process number: 2019/25765-6. R.S. thanks to FAPESP (Grant 2017/12582-5 and 2021/01357-6). L.S. thanks FAPESP (grant 2020/04401-5). R.F.M, R.S., L.S., P.E.M., and A.F.N. gratefully acknowledge the support from the FAPESP (Grant 2017/11986-5) and Shell and the strategic importance of the support given by ANP (Brazil's National Oil, Natural Gas, and Biofuels Agency) through the R&D levy regulation. M.A. acknowledges support by the US Department of Energy, Office of Science, Office of Basic Energy Sciences, Materials Sciences and Engineering Division under Contract No. DE-AC02-05-CH11231 (D2S2 program KCD2S2). *Work at the Molecular Foundry was supported by the Office of Science, Office of Basic Energy Sciences, of the U.S. Department of Energy under Contract No. DE-AC02-05CH11231.*

Received: ((will be filled in by the editorial staff))

Revised: ((will be filled in by the editorial staff))

Published online: ((will be filled in by the editorial staff))

References

[1] T. Wu, Z. Qin, Y. Wang, Y. Wu, W. Chen, S. Zhang, M. Cai, S. Dai, J. Zhang, J. Liu, Z. Zhou, X. Liu, H. Segawa, H. Tan, Q. Tang, J. Fang, Y. Li, L. Ding, Z. Ning, Y. Qi, Y. Zhang, L. Han, *Nano-Micro Lett.* **2021**, *13*, 152.

[2] S. Ma, G. Yuan, Y. Zhang, N. Yang, Y. Li, Q. Chen, *Energy Environ. Sci.* **2022**, *15*, 13.

[3] P. Wang, Y. Wu, B. Cai, Q. Ma, X. Zheng, W.-H. Zhang, *Adv. Funct. Mater.* **2019**, *29*, 1807661.

[4] Perovskites take steps to industrialization, *Nat. Energy* **2020**, *5*, 1.

[5] M. Saliba, T. Matsui, J.-Y. Seo, K. Domanski, J.-P. Correa-Baena, M. Khaja Nazeeruddin, S. M. Zakeeruddin, W. Tress, A. Abate, A. Hagfeldt, M. Grätzel, *Energy Environ. Sci.* **2016**, *9*, 1989.

[6] M. Saliba, T. Matsui, K. Domanski, J.-Y. Seo, A. Ummadisingu, S. M. Zakeeruddin, J.-P. Correa-Baena, W. R. Tress, A. Abate, A. Hagfeldt, M. Grätzel, *Science* **2016**, *354*, 206.

[7] M. Grätzel, *Acc. Chem. Res.* **2017**, *50*, 487.

[8] W. Tan, A. R. Bowring, A. C. Meng, M. D. McGehee, P. C. McIntyre, *ACS Appl. Mater. Interfaces* **2018**, *10*, 5485.

[9] Y.-W. Jang, S. Lee, K. M. Yeom, K. Jeong, K. Choi, M. Choi, J. H. Noh, *Nat. Energy* **2021**, *6*, 63.

[10] J. J. Yoo, S. Wieghold, M. C. Sponseller, M. R. Chua, S. N. Bertram, N. T. Putri Hartono, J. S. Tresback, E. C. Hansen, J.-P. Correa-Baena, V. Bulović, T. Buonassisi, S. Sik Shin, M. G. Bawendi, *Energy Environ. Sci.* **2019**, *12*, 2192.

[11] A. H. Proppe, A. Johnston, S. Teale, A. Mahata, R. Quintero-Bermudez, E. H. Jung, L. Grater, T. Cui, T. Filleter, C.-Y. Kim, S. O. Kelley, F. De Angelis, E. H. Sargent, *Nat. Commun.* **2021**, *12*, 3472.

[12] Q. Jiang, Y. Zhao, X. Zhang, X. Yang, Y. Chen, Z. Chu, Q. Ye, X. Li, Z. Yin, J. You, *Nat. Photonics* **2019**, *13*, 460.

[13] C. M. Mauck, W. A. Tisdale, *Trends Chem.* **2019**, *1*, 380.

[14] C. Ma, C. Leng, Y. Ji, X. Wei, K. Sun, L. Tang, J. Yang, W. Luo, C. Li, Y. Deng, S. Feng, J. Shen, S. Lu, C. Du, H. Shi, *Nanoscale* **2016**, *8*, 18309.

[15] A. A. Sutanto, R. Szostak, N. Drigo, V. I. E. Queloz, P. E. Marchezi, J. C. Germino, H. C. N. Tolentino, M. K. Nazeeruddin, A. F. Nogueira, G. Grancini, *Nano Lett.* **2020**, *20*, 3992.

[16] A. A. Sutanto, P. Caprioglio, N. Drigo, Y. J. Hofstetter, I. Garcia-Benito, V. I. E. Queloz, D. Neher, M. K. Nazeeruddin, M. Stolterfoht, Y. Vaynzof, G. Grancini, *Chem* **2021**, *7*, 1903.

[17] J. Gong, M. Hao, Y. Zhang, M. Liu, Y. Zhou, *Angew. Chem. Int. Ed.* **2022**, *61*, e202112022.

[18] M. S. de Holanda, R. Szostak, P. E. Marchezi, L. G. T. A. Duarte, J. C. Germino, T. D. Z. Atvars, A. F. Nogueira, *Sol. RRL* **2019**, *3*, 1900199.

[19] C. Lan, Z. Zhou, R. Wei, J. C. Ho, *Mater. Today Energy* **2019**, *11*, 61.

[20] S. G. Motti, T. Crothers, R. Yang, Y. Cao, R. Li, M. B. Johnston, J. Wang, L. M. Herz, *Nano Lett.* **2019**, *19*, 3953.

[21] C. Ge, Y. Z. B. Xue, L. Li, B. Tang, H. Hu, *Front. Mater.* **2020**, *7*.

[22] S. Kumar, L. Houben, K. Rechav, D. Cahen, *Proc. Natl. Acad. Sci.* **2022**, *119*, e2114740119.

[23] X. Li, J. M. Hoffman, M. G. Kanatzidis, *Chem. Rev.* **2021**, *121*, 2230.

[24] F. Li, Y. Xie, Y. Hu, M. Long, Y. Zhang, J. Xu, M. Qin, X. Lu, M. Liu, *ACS Energy Lett.* **2020**, *5*, 1422.

[25] B. P. Kore, W. Zhang, B. W. Hoogendoorn, M. Safdari, J. M. Gardner, *Commun. Mater.* **2021**, *2*, 1.

[26] X. Liu, T. Webb, L. Dai, K. Ji, J. A. Smith, R. C. Kilbride, M. Yavari, J. Bi, A. Ren, Y. Huang, Z. Wang, Y. Shen, G. Shao, S. J. Sweeney, S. Hinder, H. Li, D. G. Lidzey, S. D. Stranks, N. C. Greenham, S. R. P. Silva, W. Zhang, *ENERGY Environ. Mater. n/a*.

[27] H.-C. Chen, J.-M. Lan, H.-L. Hsu, C.-W. Li, T.-S. Shieh, K.-T. Wong, C.-P. Chen, *Mater. Chem. Front.* **2021**, *5*, 3378.

[28] G. Liu, H. Zheng, H. Xu, L. Zhang, X. Xu, S. Xu, X. Pan, *Nano Energy* **2020**, *73*, 104753.

[29] A. Bala, V. Kumar, *ACS Appl. Energy Mater.* **2021**, *4*, 1860.

[30] L. He, H. Wu, X. Lian, L. Zuo, G. Wu, H. Chen, *Org. Electron.* **2021**, *92*, 106124.

[31] J. Xi, J. Byeon, U. Kim, K. Bang, G. R. Han, J.-Y. Kim, J. Yoon, H. Dong, Z. Wu, G. Divitini, K. Xi, J. Park, T.-W. Lee, S. K. Kim, M. Choi, J. W. Lee, *Ener. Environ. Sci.* **2021**, *14*, 4915-4925.

[32] H. Su, J. Zhang, Y. Hu, X. Du, Y. Yang, J. You, L. Gao, S. (Frank) Liu, *Adv. Energy Mater.* **2021**, *11*, 2101454.

[33] J. Xi, I. Spanopoulos, K. Bang, J. Xu, H. Dong, Y. Yang, C. D. Malliakas, J. M. Hoffman, M. G. Kanatzidis, Z. Wu, *J. Am. Chem. Soc.* **2020**, *142*, 19705.
[34] T. Niu, J. Lu, X. Jia, Z. Xu, M.-C. Tang, D. Barrit, N. Yuan, J. Ding, X. Zhang, Y. Fan, T. Luo, Y. Zhang, D.-M. Smilgies, Z. Liu, A. Amassian, S. Jin, K. Zhao, S. Liu, *Nano Lett.* **2019**, *19*, 7181.
[35] H. Chen, S. Teale, B. Chen, Y. Hou, L. Grater, T. Zhu, K. Bertens, S. M. Park, H. R. Atapattu, Y. Gao, M. Wei, A. K. Johnston, Q. Zhou, K. Xu, D. Yu, C. Han, T. Cui, E. H. Jung, C. Zhou, W. Zhou, A. H. Proppe, S. Hoogland, F. Laquai, T. Filleter, K. R. Graham, Z. Ning, E. H. Sargent, *Nat. Photonics* **2022**, 1.
[36] C. Liu, Y. Yang, K. Rakstys, A. Mahata, M. Franckevicius, E. Mosconi, R. Skackauskaite, B. Ding, K. G. Brooks, O. J. Usiobo, J.-N. Audinot, H. Kanda, S. Driukas, G. Kavaliauskaite, V. Gulbinas, M. Dessimoz, V. Getautis, F. De Angelis, Y. Ding, S. Dai, P. J. Dyson, M. K. Nazeeruddin, *Nat. Commun.* **2021**, *12*, 6394.
[37] F. S. Ghoreishi, V. Ahmadi, R. Poursalehi, M. SamadPour, M. B. Johansson, G. Boschloo, E. M. J. Johansson, *J. Power Sources* **2020**, *473*, 228492.
[38] Y. Hu, J. Schlipf, M. Wussler, M. L. Petrus, W. Jaegermann, T. Bein, P. Müller-Buschbaum, P. Docampo, *ACS Nano* **2016**, *10*, 5999.
[39] F. Fiorentino, M. D. Albaqami, I. Poli, A. Petrozza, *ACS Appl. Mater. Interfaces* **2021**.
[40] W. Fan, Y. Shen, K. Deng, Q. Chen, Y. Bai, *J. Mater. Chem. A* **2021**, *9*, 26829.
[41] A. A. Sutanto, N. Drigo, V. I. E. Queloz, I. Garcia-Benito, A. R. Kirmani, L. J. Richter, P. A. Schouwink, K. Taek Cho, S. Paek, M. Khaja Nazeeruddin, G. Grancini, *J. Mater. Chem. A* **2020**, *8*, 2343.
[42] X.-H. Zhu, N. Mercier, A. Riou, P. Blanchard, P. Frère, *Chem. Commun.* **2002**, 2160.
[43] M. A. Green, Y. Jiang, A. M. Soufiani, A. Ho-Baillie, *J. Phys. Chem. Lett.* **2015**, *6*, 4774.
[44] O. Yaffe, A. Chernikov, Z. M. Norman, Y. Zhong, A. Velauthapillai, A. van der Zande, J. S. Owen, T. F. Heinz, *Phys. Rev. B* **2015**, *92*, 045414.
[45] F. Babbe, C. M. Sutter-Fella, *Adv. Energy Mater.* **2020**, *10*, 1903587.
[46] C. Zhang, S. Wu, L. Tao, G. M. Arumugam, C. Liu, Z. Wang, S. Zhu, Y. Yang, J. Lin, X. Liu, R. E. I. Schropp, Y. Mai, *Adv. Energy Mater.* **2020**, *10*, 2002004.
[47] J. Li, X. Yuan, P. Jing, J. Li, M. Wei, J. Hua, J. Zhao, L. Tian, *RSC Adv.* **2016**, *6*, 78311.
[48] E. T. Hoke, D. J. Slotcavage, E. R. Dohner, A. R. Bowring, H. I. Karunadasa, M. D. McGehee, *Chem. Sci.* **2015**, *6*, 613.
[49] M. Yuan, L. N. Quan, R. Comin, G. Walters, R. Sabatini, O. Voznyy, S. Hoogland, Y. Zhao, E. M. Beauregard, P. Kanjanaboos, Z. Lu, D. H. Kim, E. H. Sargent, *Nat. Nanotechnol.* **2016**, *11*, 872.
[50] R. F. Moral, L. G. Bonato, J. C. Germino, W. X. Coelho Oliveira, R. Kamat, J. Xu, C. J. Tassone, S. D. Stranks, M. F. Toney, A. F. Nogueira, *Chem. Mater.* **2019**, *31*, 9472.
[51] T. Moot, J. B. Patel, G. McAndrews, E. J. Wolf, D. Morales, I. E. Gould, B. A. Rosales, C. C. Boyd, L. M. Wheeler, P. A. Parilla, S. W. Johnston, L. T. Schelhas, M. D. McGehee, J. M. Luther, *ACS Energy Lett.* **2021**, *6*, 2038.
[52] C. Katan, N. Mercier, J. Even, *Chem. Rev.* **2019**, *119*, 3140.
[53] J.-H. Lee, N. C. Bristowe, J. H. Lee, S.-H. Lee, P. D. Bristowe, A. K. Cheetham, H. M. Jang, *Chem. Mater.* **2016**, *28*, 4259.
[54] W.-J. Wei, C. Li, L.-S. Li, Y.-Z. Tang, X.-X. Jiang, Z.-S. Lin, *J. Mater. Chem. C* **2019**, *7*, 11964.
[55] O. F. Williams, Z. Guo, J. Hu, L. Yan, W. You, A. M. Moran, *J. Chem. Phys.* **2018**, *148*, 134706.
[56] V. Gold, Ed., *The IUPAC Compendium of Chemical Terminology: The Gold Book*, 4th ed., International Union of Pure and Applied Chemistry (IUPAC), Research Triangle Park, NC, **2019**.
[57] C. M. M. Soe, G. P. Nagabhushana, R. Shivaramaiah, H. Tsai, W. Nie, J.-C. Blancon, F. Melkonyan, D. H. Cao, B. Traoré, L. Pedesseau, M. Kepenekian, C. Katan, J. Even, T. J. Marks, A. Navrotsky, A. D. Mohite, C. C. Stoumpos, M. G. Kanatzidis, *Proc. Natl. Acad. Sci.* **2019**, *116*, 58.
[58] B. Wang, K. Young Wong, X. Xiao, T. Chen, *Sci. Rep.* **2015**, *5*, 10557.
[59] L. N. Quan, M. Yuan, R. Comin, O. Voznyy, E. M. Beauregard, S. Hoogland, A. Buin, A. R. Kirmani, K. Zhao, A. Amassian, D. H. Kim, E. H. Sargent, *J. Am. Chem. Soc.* **2016**, *138*, 2649.
[60] J. Xing, Y. Zhao, M. Askerka, L. N. Quan, X. Gong, W. Zhao, J. Zhao, H. Tan, G. Long, L. Gao, Z. Yang, O. Voznyy, J. Tang, Z.-H. Lu, Q. Xiong, E. H. Sargent, *Nat. Commun.* **2018**, *9*, 3541.

[61] M.-G. La-Placa, L. Gil-Escrig, D. Guo, F. Palazon, T. J. Savenije, M. Sessolo, H. J. Bolink, *ACS Energy Lett.* **2019**, *4*, 2893.
[62] M. A. Green, *Solid-State Electron.* **1981**, *24*, 788.
[63] R. Azmi, E. Ugur, A. Seitkhan, F. Aljamaan, A. S. Subbiah, J. Liu, G. T. Harrison, M. I. Nugraha, M. K. Eswaran, M. Babics, Y. Chen, F. Xu, T. G. Allen, A. ur Rehman, C.-L. Wang, T. D. Anthopoulos, U. Schwingenschlögl, M. De Bastiani, E. Aydin, S. De Wolf, *Science* **2022**, *376*, 73.
[64] T. Kodalle, T. Bertram, R. Schlatmann, C. A. Kaufmann, *IEEE J. Photovolt.* **2019**, *9*, 1839.
[65] T. Kodalle, H. A. Yetkin, A. V. Tovar, T. Bertram, R. Klenk, R. Schlatmann, C. A. Kaufmann, *IEEE J. Photovolt.* **2021**, *11*, 232.
[66] M. C. Gélvez-Rueda, M. B. Fridriksson, R. K. Dubey, W. F. Jager, W. van der Stam, F. C. Grozema, *Nat. Commun.* **2020**, *11*, 1901.
[67] J. V. Passarelli, C. M. Mauck, S. W. Winslow, C. F. Perkinson, J. C. Bard, H. Sai, K. W. Williams, A. Narayanan, D. J. Fairfield, M. P. Hendricks, W. A. Tisdale, S. I. Stupp, *Nat. Chem.* **2020**, *12*, 672.
[68] G. Kim, H. Min, K. S. Lee, D. Y. Lee, S. M. Yoon, S. I. Seok, *Science* **2020**, *370*, 108.
[69] T. Zhu, D. Zheng, J. Liu, L. Coolen, T. Pauporté, *ACS Appl. Mater. Interfaces* **2020**, *12*, 37197.

ToC Entry:

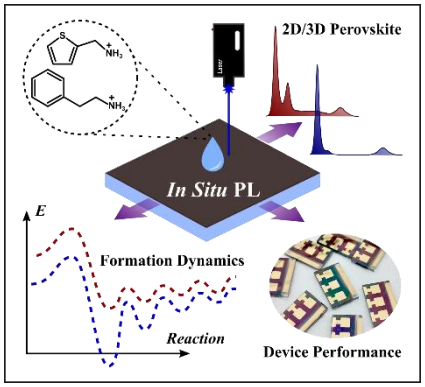

We use in-situ photoluminescence measurements to elucidate the formation dynamics of 2D Ruddlesden-Popper phases on triple cation perovskite films using two different molecules (PEAI and TMAI). We find that the formation dynamics and final composition of the RP-phases depend on the molecule used, opening opportunities to optimize the 2D-passivation mechanisms individually and finally improving solar cell efficiency.

Supporting Information

Revealing the transient formation dynamics and optoelectronic properties of 2D Ruddlesden-Popper phases on 3D perovskites

Tim Kodalle, Raphael F. Moral, Lucas Scalon, Rodrigo Szostak, Maged Abdelsamie, Paulo Ernesto Marchezi, Ana F. Nogueira, Carolin M. Sutter-Fella**

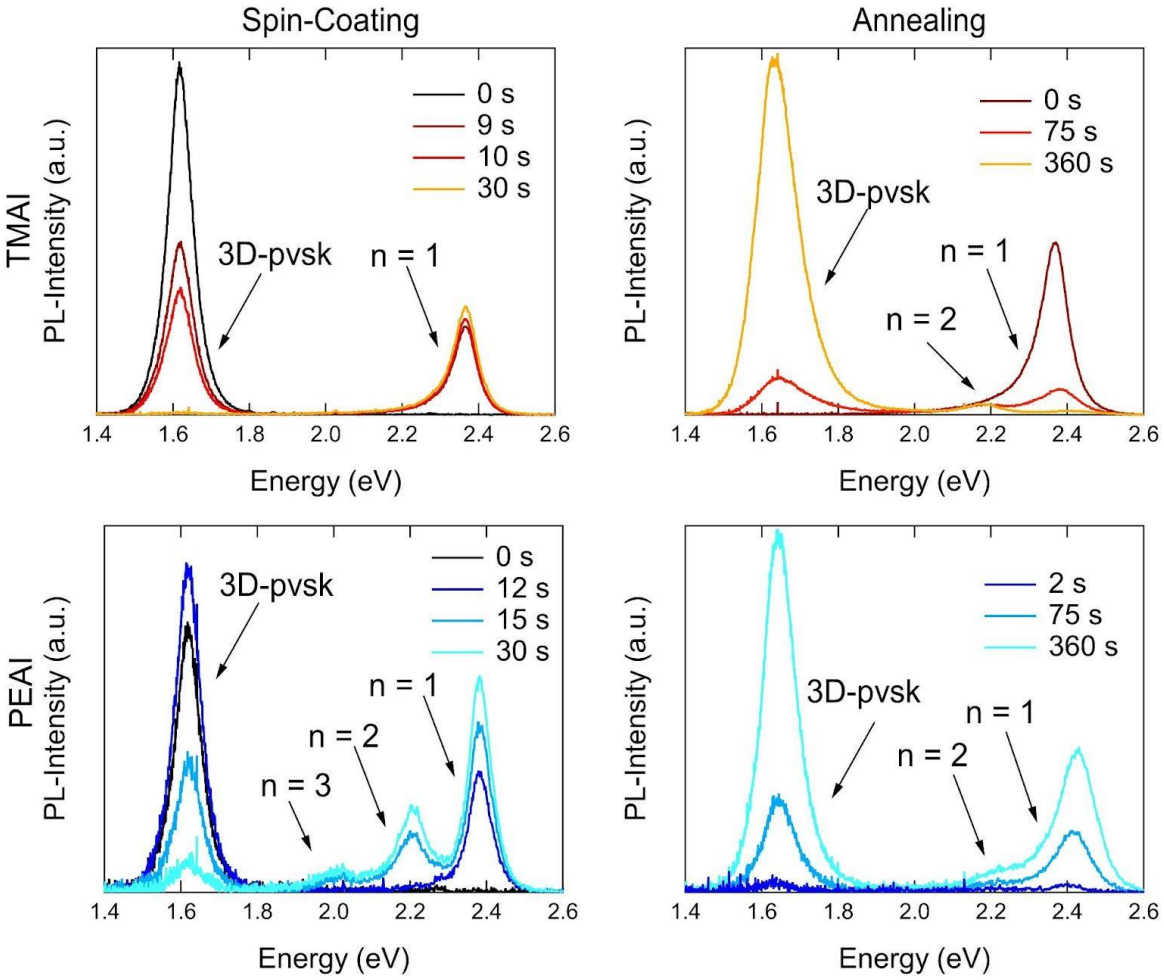

Figure S1. Individual PL spectra of crucial points in time from the *in situ* PL measurements during spin-coating and annealing for TMAI and PEAI treated perovskites.

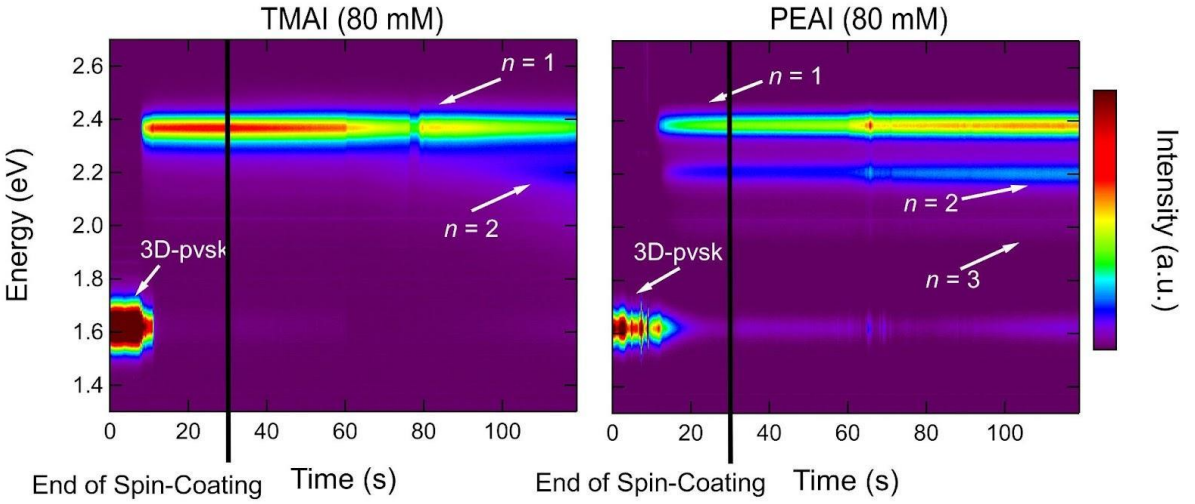

Figure S2. Extended *in situ* PL measurements (TMAI-80 and PEAI-80) during and after the spin-coating including the drying process of the films. It is clearly visible that there is a conversion from n = 1 to n = 2 during the drying process in the case of TMAI.

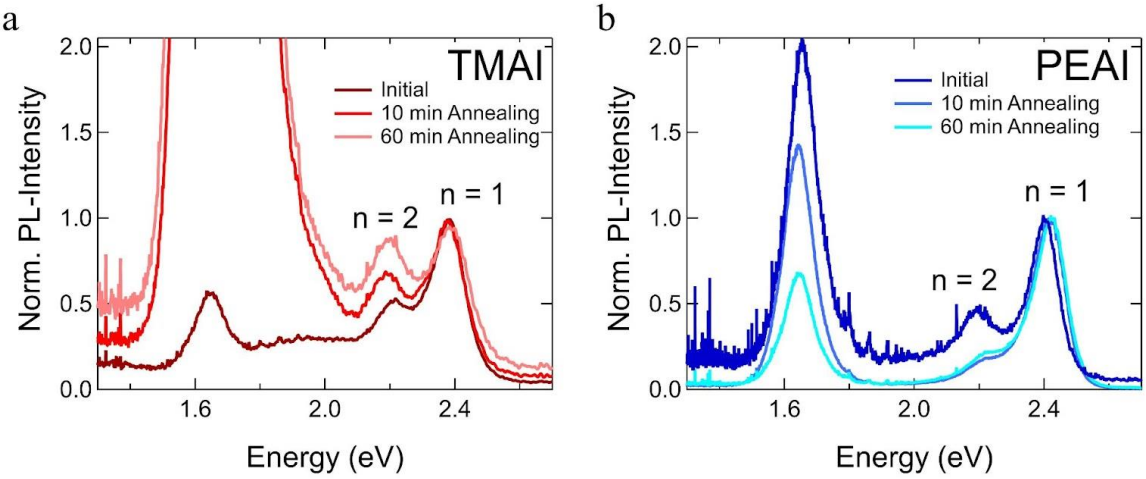

Figure S3. Steady State PL (SSPL) spectra of TMAI (a) and PEAI (b) treated samples measured during a prolonged annealing step of 60 minutes at 100C. Note that the samples were treated with 80 mM of the respective molecule and all spectra were normalized to the intensity of the respective n = 1 peak. The initial measurements were taken about 10s after the beginning of the annealing in order to let the sample heat up to 100C.

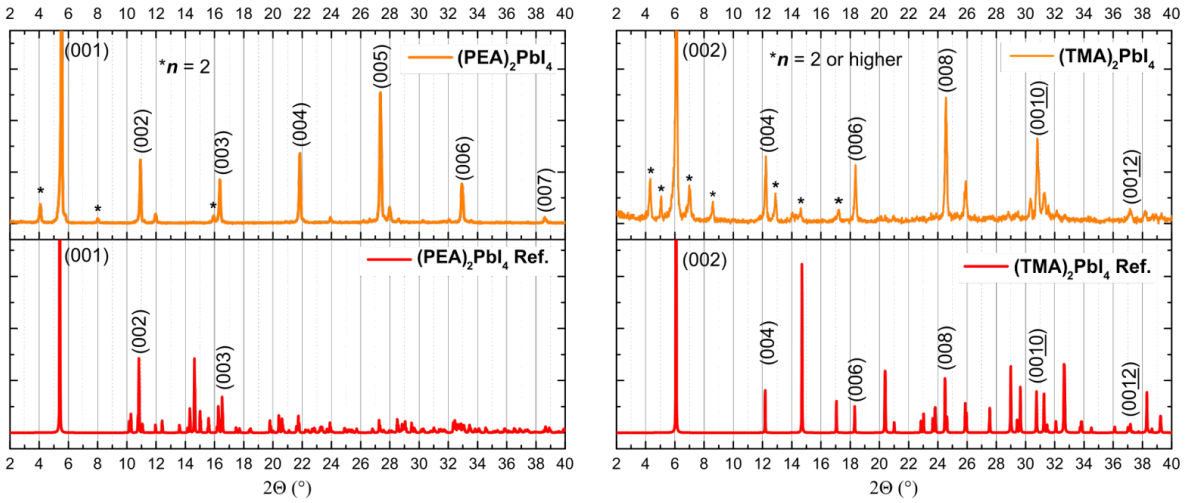

Figure S4. Powder XRD of the PEAI and TMAI RP-phases obtained in the solution-process synthesis. The yellow diffractograms are the experimental data. Even though the color of the materials is red after the synthesis, the majority of the powder is composed by the n = 1 phase in both cases. For PEAI, the ratio n = 1/n = 2 is high, and only minimal amounts of n = 2 phases are present. In the case of TMAI, we see diffraction of the n ≥ 2 phases, and the ratio n = 1/n ≥ 2 is lower than in the case of PEAI. Note that, even in the powder, avoiding preferential orientation of these materials is difficult because of its 2D morphology; therefore, the Bragg reflections in the direction [00*l*] are very intense in comparison to the other diffractions.

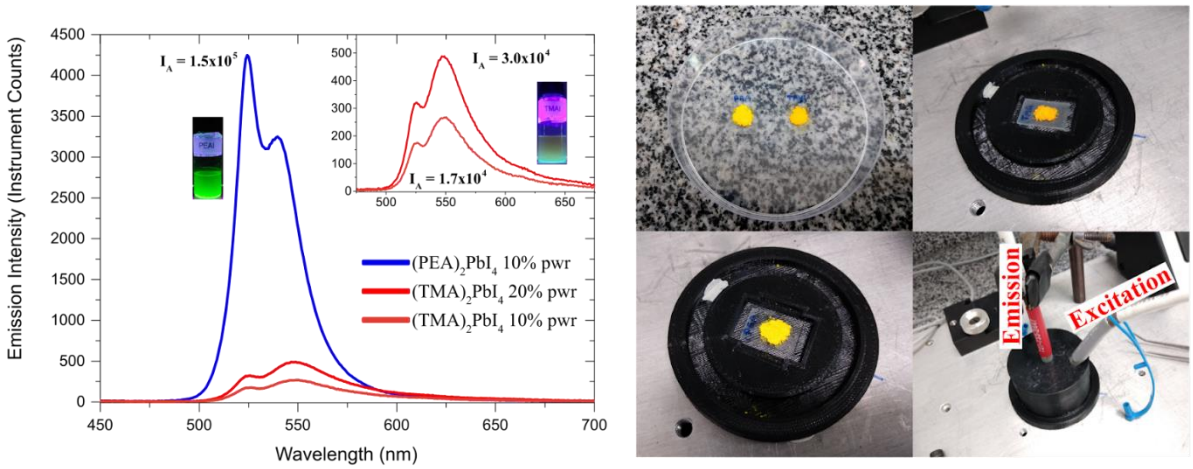

Figure S5. a) Steady-state PL measurements of the $(PEA)_2PbI_4$ and $(TMA)_2PbI_4$ materials synthesized *via* adapted solution process method.[1] The inset photos show the materials in their reaction solution under UV light. The integrated PL intensity (I_A) of $(PEA)_2PbI_4$ ($1.5x10^5$) is nearly one order of magnitude higher than I_A for $(TMA)_2PbI_4$ ($1.7x10^4$) when both are excited with the same power density set to 10 % of the maximum of the LED used (365 nm). Even increasing the LED power to 20%, the $(TMA)_2PbI_4$ integrated intensity is much lower than the integrated intensity of $(PEA)_2PbI_4$ at 10% power. **b)** Images of the samples and the measurement setup showing how the PL spectra were measured. The amount of material in both samples was 0.016 mmol (~15 mg each). The dual-band profile of the emission in these pure n = 1 RP-phases is due to strong exciton-phonon coupling in these materials. This emission profile has been thoroughly discussed in recent works.[2-4]

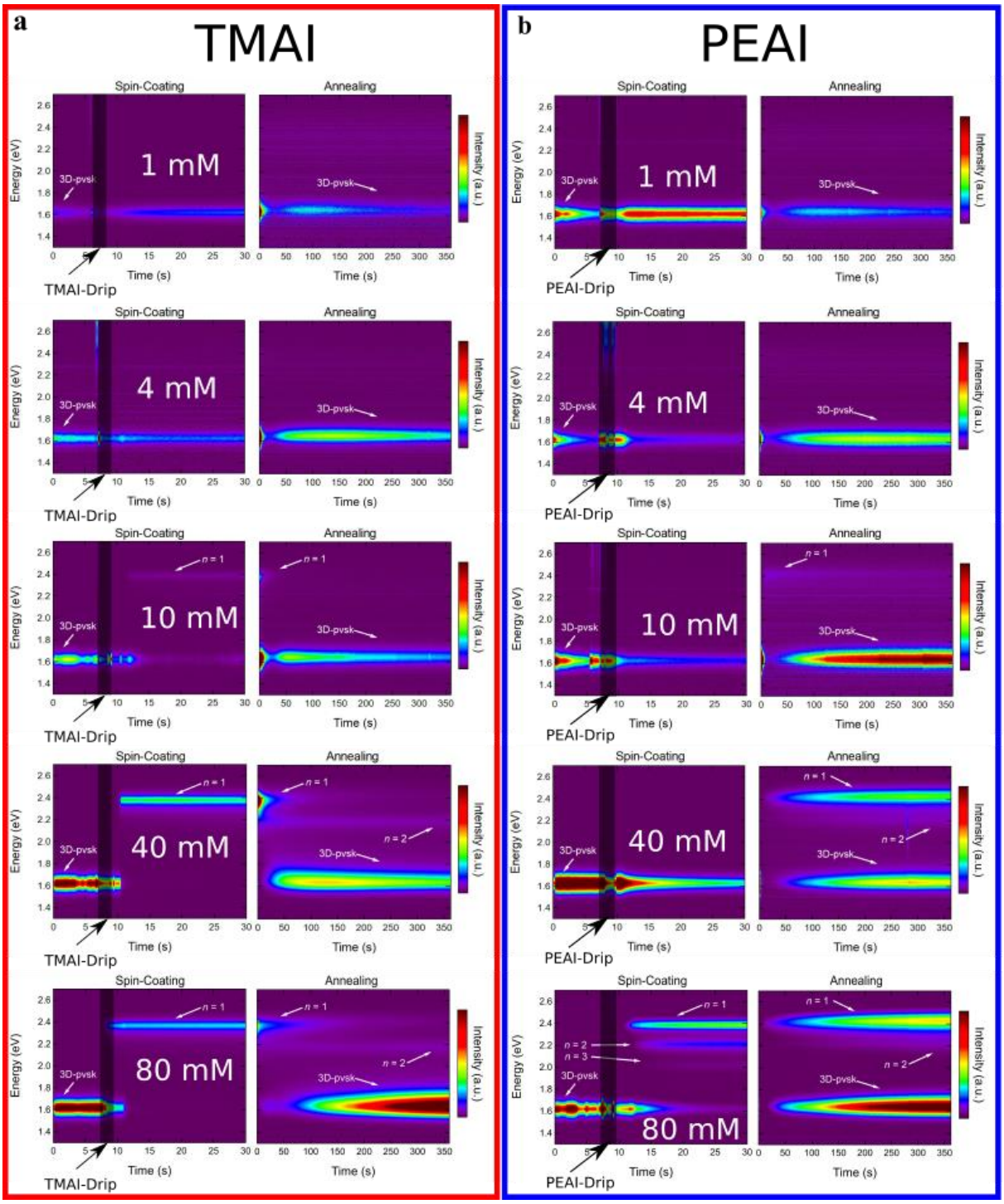

Figure S6. a) Contour plots of *in situ* PL measured during spin coating and subsequent annealing of samples treated with varied TMAI-concentration (80 mM to 1 mM in IPA). b) Contour plots of *in situ* PL measured during spin coating and subsequent annealing of samples treated with varied PEAI-concentration (80 mM to 1 mM in IPA).

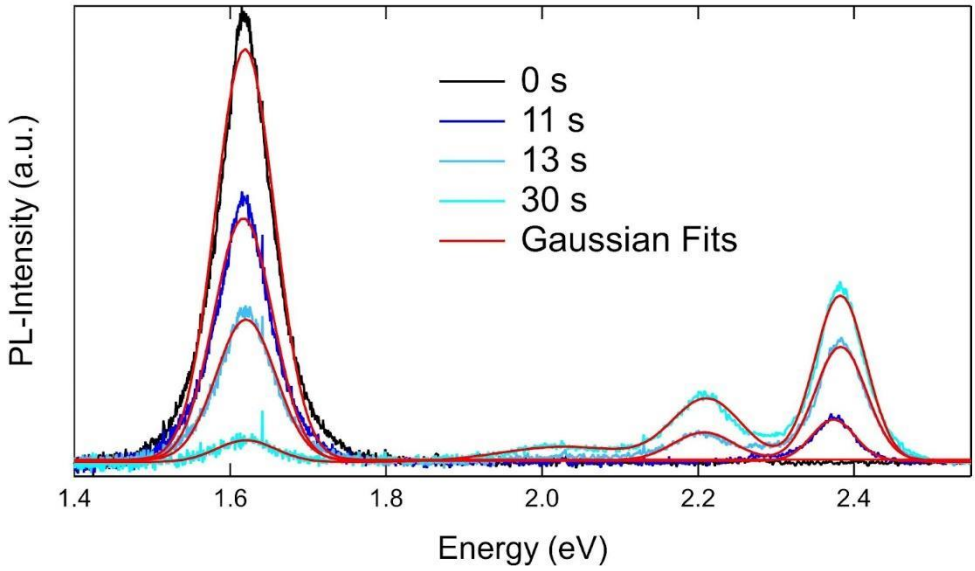

Figure S7. Examples of the Gaussian fit to the PL curves of the PEAI-80 sample. Spectra are taken from the respective timepoints during spin-coating.

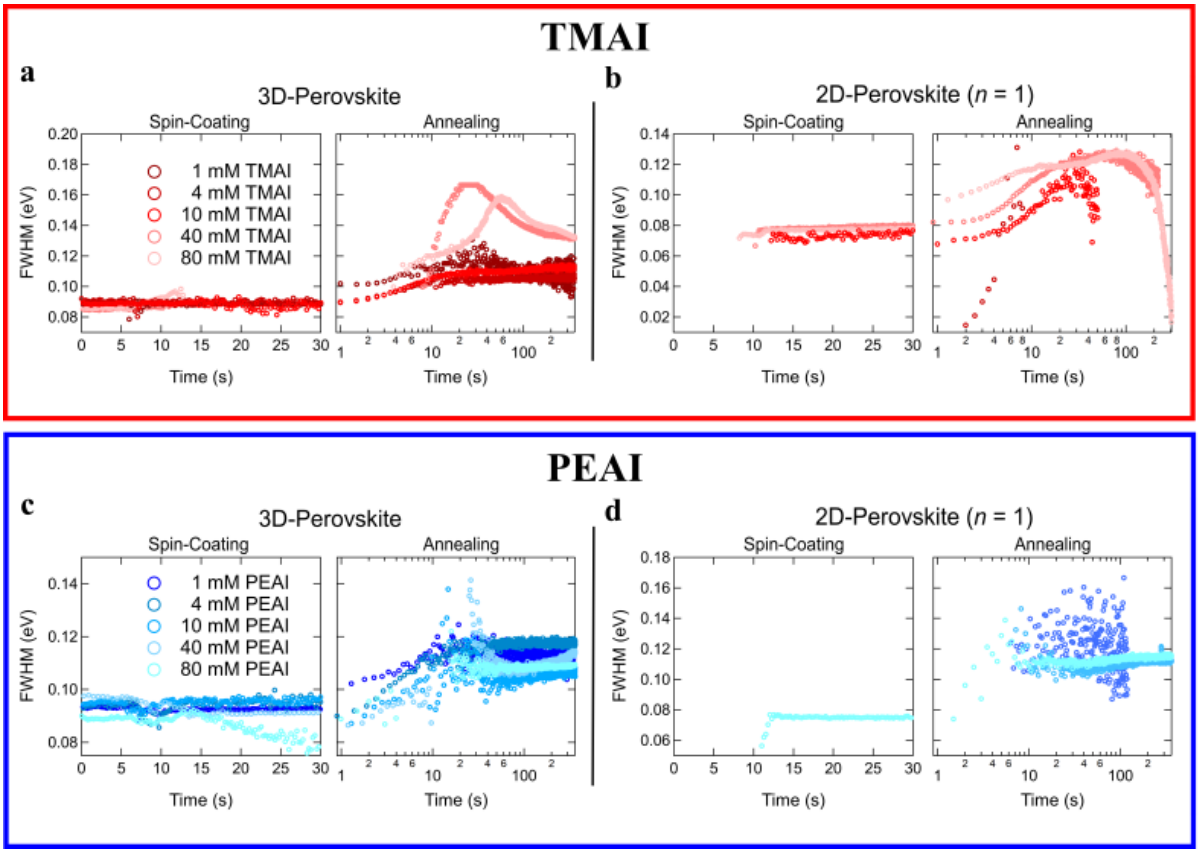

Figure S8. a) Evolution of the FWHM of the PL-peak corresponding to the 3D-pvsk, and **b)** evolution of the FWHM of the PL-peak corresponding to the n = 1 RP-phase during spin-coating and annealing of TMAI-treated 3D-pvsk films. **c)** and **d)** show the corresponding plots for PEAI-treated films. Note that not all samples show peaks related to the RP-phases (at all times) and they are consequently missing in some of these panels.

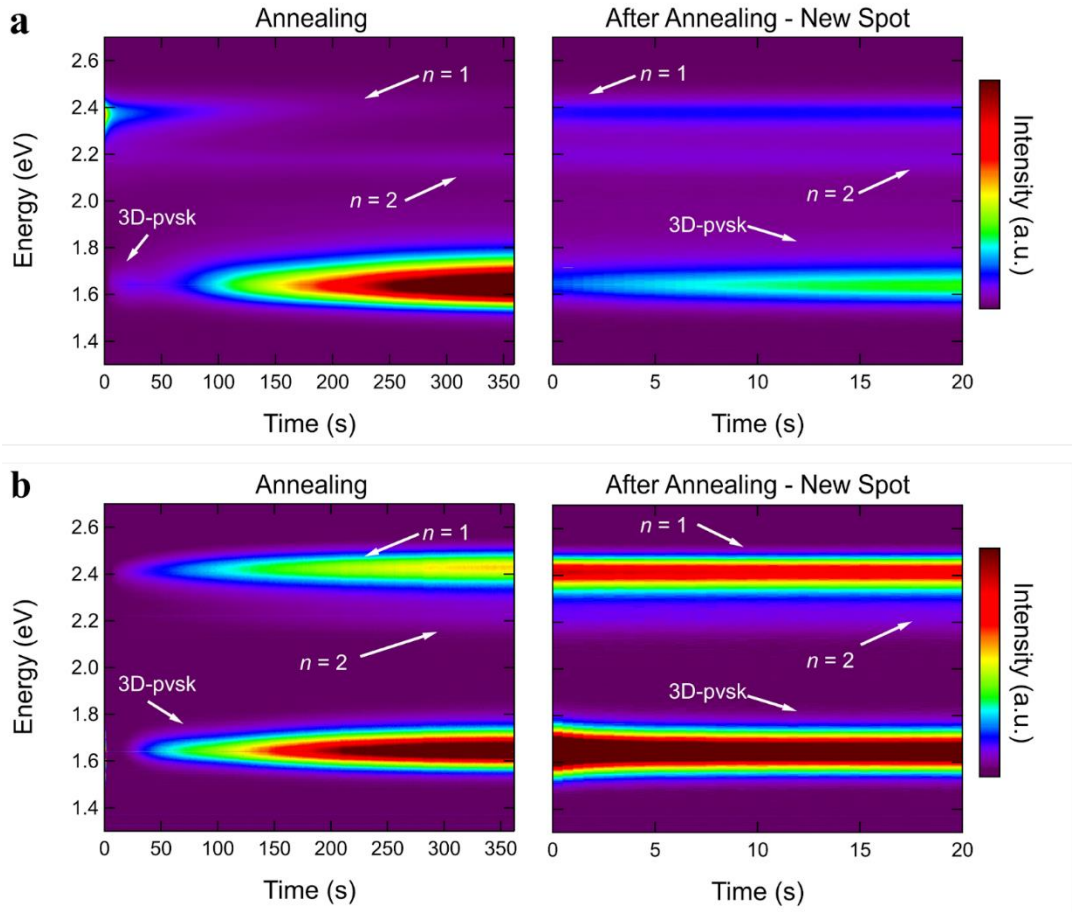

Figure S9. Influence of the laser illumination on the PL spectra taken during the annealing. Since the substrate is spinning under the laser during spin-coating, strongly reducing the illumination time for each spot on the illuminated circle, it is safe to assume that the effect of the laser on the PL-spectra is bigger during the annealing. Panel **a)** shows the evolution of the PL spectra of the TMAI-80 sample during spin coating (left) and measured on a second spot, which has not been illuminated, during the annealing of the same sample right after the annealing (right). Panel **b)** shows the same for the PEAI-80 sample. In both cases, the steady illumination with the laser does not lead to the appearance or disappearance of any PL peaks but induces a slight degradation of the sample surface. In the case of TMAI, where the salt has been completely converted to RP-phases during spin-coating, the laser accelerates the degradation of the RP-phases and the corresponding re-emerging of the 3D-pvsk-peak. In the case of PEAI, where the salt is not completely converted during the spin-coating, the laser reduces the intensity-increase of the RP-phases during annealing - presumably because part of the RP-phases are degrading under the constant illumination, while there is still salt being converted. It should be kept in mind, though, that lateral inhomogeneities might also influence the intensity of the PL peaks. In summary, we think it is reasonable to neglect the effect of the laser on the phenomena described in the main article.

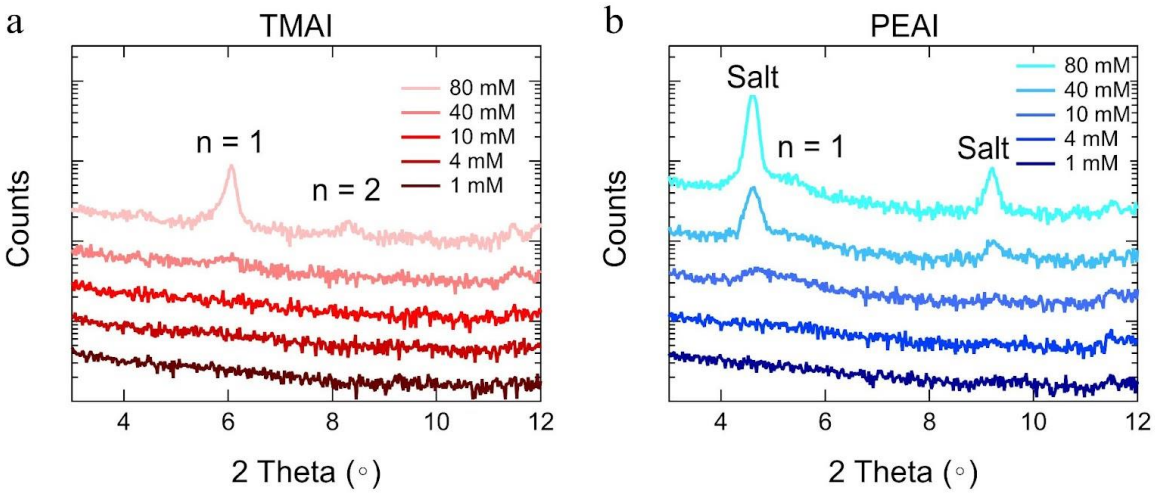

Figure S10. X-ray diffraction patterns of samples treated with TMAI (a) and PEAI (b) taken after dynamic deposition of the respective molecule but before annealing. In the case of TMAI, there is no trace of unreacted salt present, even at the highest concentration, while in case of PEAI, there are traces of unreacted salt present for concentrations > 4 mM. The latter is in good agreement with the evolution of the PL-intensity of the n = 1 peak in **Figure 2d**.

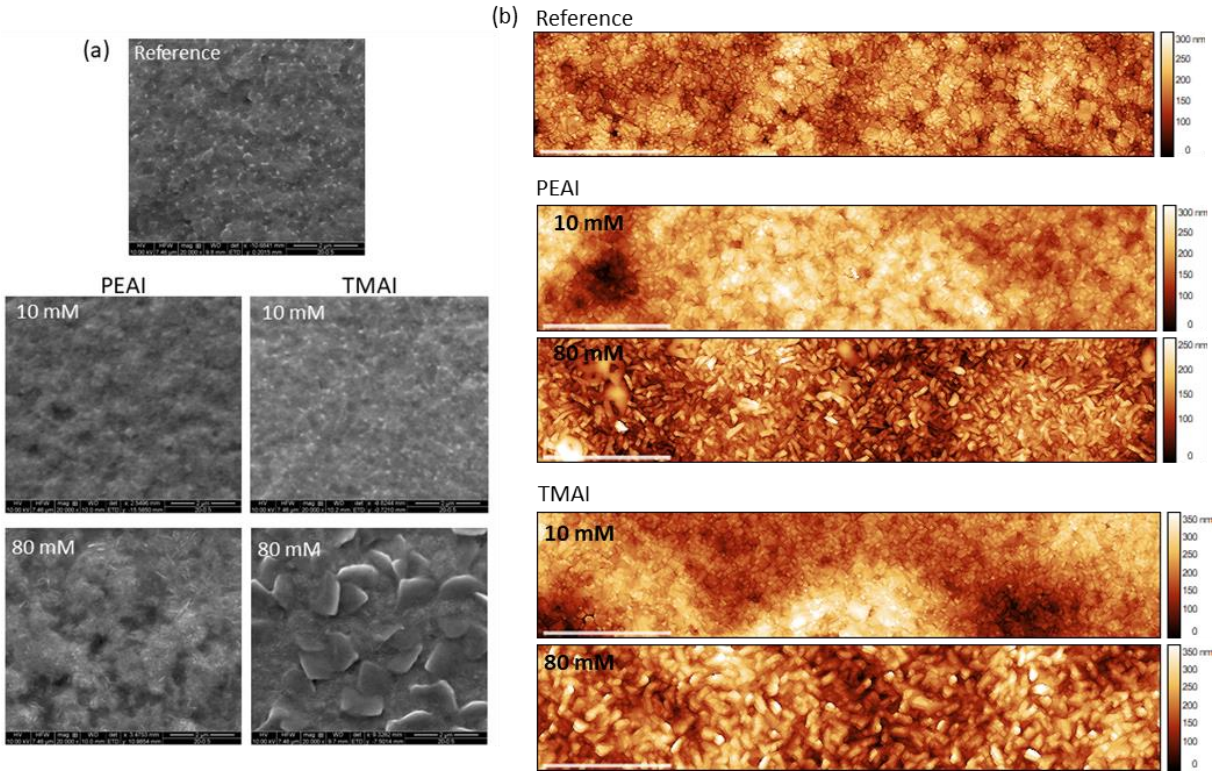

Figure S11. (a) Scanning electron microscopy images and (b) Atomic force microscopy of the pristine perovskite film with PEAI and TMAI dripping. The root means square roughness (S_q) varies from 60 nm, for the control; 48 and 39 nm, for PEAI-10 and -80, respectively; 60 and 61 nm, for TMAI-10 and -80, respectively.

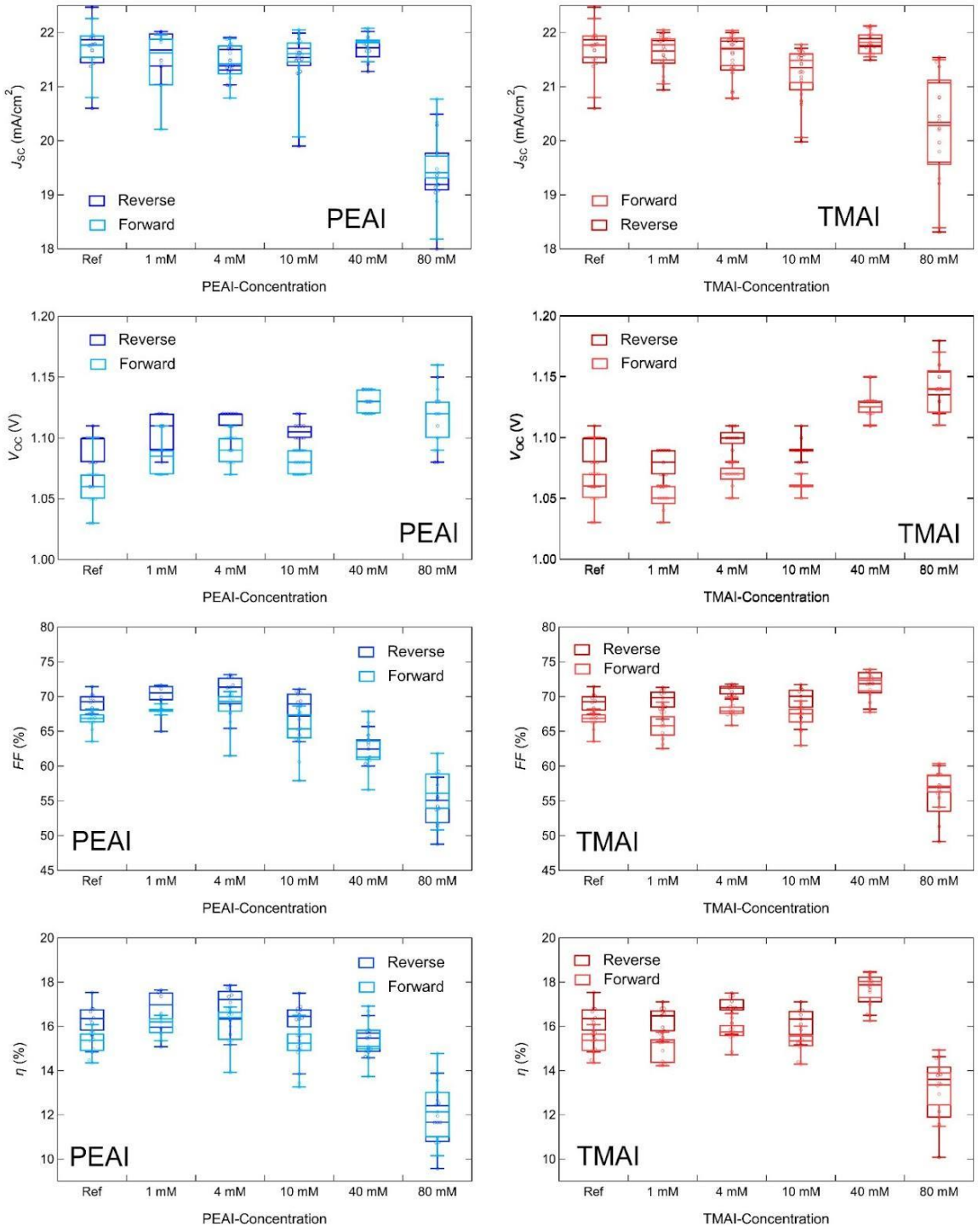

Figure S12. Boxplots of the PV parameters of the solar cell devices treated with varying concentrations of PEAI or TMAI respectively.

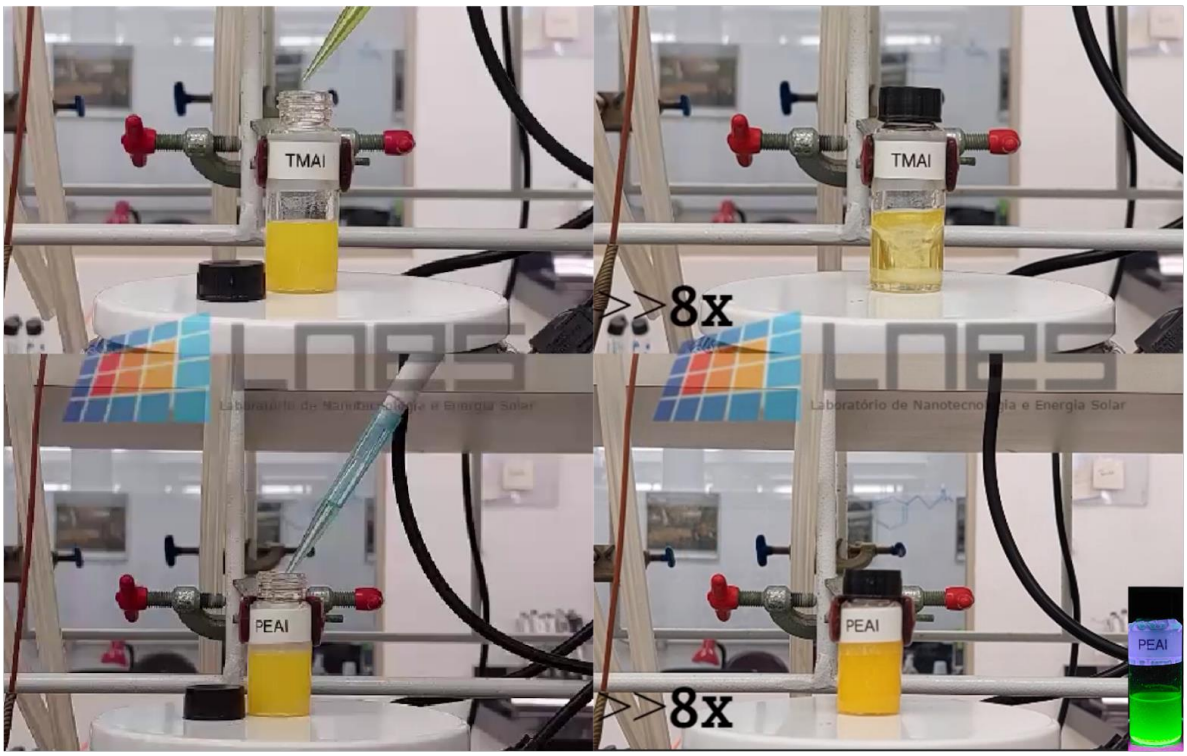

Figure S13. Selected images of the solution-process reaction between PbI_2 and the amines, phenylethylamine, and 2-thiophenemethylamine. After 2.40 minutes, the TMAI reaction is a clear yellow solution, while the PEAI reaction is completed and the $(PEA)_2PbI_4$ (n = 1) RP-phase is formed. The evidence for the reaction completion is the flask under UV light (inset) with the characteristic green emission of this material. This visual experiment shows the equilibrium between all the precursors solubilized and the crystal formation. For PEAI, the equilibrium is highly shifted to crystallization, instead of all dissolved. For TMAI, the equilibrium is slightly shifted for all the precursors dissolved rather than crystallization. This shows that the $(PEA)_2PbI_4$ has more negative formation energy compared to $(TMA)_2PbI_4$. For the entire video, see **Supporting Video 1**.

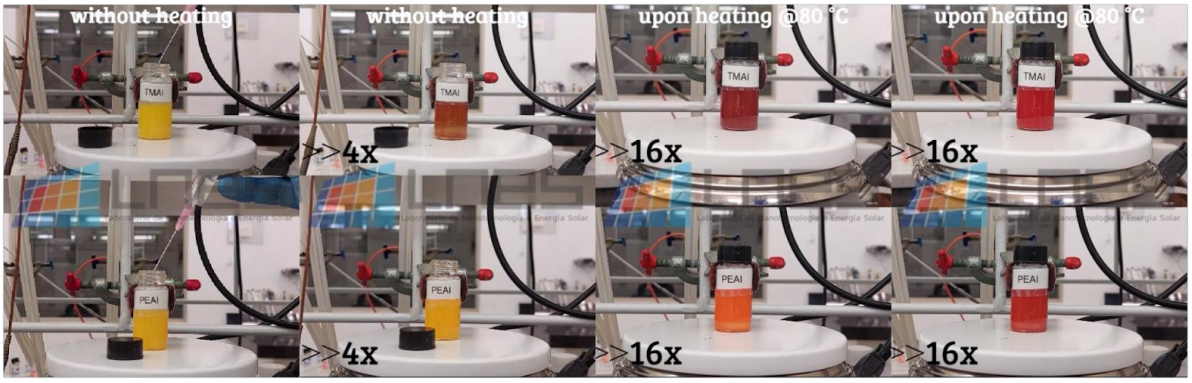

Figure S14. Selected images of the solution-process reaction between $(PEA)_2PbI_4$ and $(TMA)_2PbI_4$ with formamidinium acetate [(FA)OAc]. This experiment shows how readily the $(TMA)_2PbI_4$ reacts with FA^+ cations to form n > 1 RP-phases, characterized by the dark red colors. On the contrary, $(PEA)_2PbI_4$ requires heat and time for the reaction to occur. The final product of these reactions is a mixture of RP-phases with different values of n, as we can verify from the XRD of the powders in **Figure S4**. In the case of PEA, the main product is the n = 1

RP-phase with some low-intense n = 2 diffraction. In the case of TMA, although the n = 1 RP-phase is also predominant, we see a mixture of the n = 2 and probably the n = 3 RP-phases with considerable diffraction intensities. These experiments corroborate the energy diagrams we propose in **Figure 4** of the main text, where the energy landscape is uneven for PEAI and more evenly distributed for TMAI.

Supplementary Text 1

To qualitatively verify the hypothesis regarding the energy diagrams, we carried out a simple, visual experiment, synthesizing the relevant materials in an adapted solution-process procedure reported in the literature.[1] Basically, PbI_2 is suspended in toluene and butyric acid under intense stirring. Note that the mixture of toluene and butyric acid alone does not dissolve PbI_2. Then, the neutral amine (phenylethylamine - PEAm - or 2-thiophenemethylamine - TMAm) is added to this suspension. Upon amine addition, two reactions occur: the reaction between the amine and the butyric acid and an intercalation reaction between the amine and PbI_2.[5, 6] The first provides ammonium cations to the formation of the 2D RP-phase; the second, at least partially, causes the dissolution of PbI_2. **Supporting Video 1** shows the reactions from the moment that the amines are added, and **Figure S13** shows pictures of selected moments of this reaction.

In the case of PEAm, the dissolution reaction apparently does not occur; PbI_2 reacts directly with the PEA^+ cations to form the n = 1 RP-phase. Since both solids are yellow, there is no visual difference during the time lapse of the reaction (2.40 min.); however, a bright green emission is visible under UV-light, even when the solid is still suspended in the synthesis mixture (inset in **Figure S13**). In the case of TMAm, a clear, yellow solution is formed after the same time and, only upon gentle heat, the n = 1 RP-phase forms. These two reactions allow us to conclude that the equilibrium between $(PEA)_2PbI_4$ crystallization and all precursors in solution is shifted towards crystallization; on the contrary, in the case of TMAm, the equilibrium between crystallization of $(TMA)_2PbI_4$ and complete dissolution of precursors is only slightly dislocated to the crystallization. In comparative terms, this qualitative experiment suggests that the formation energy of the n = 1 phase for PEA^+ is lower than for its analogue TMA^+, as proposed in the energy diagrams of **Figure 4** in the main text. Also, this experiment shows that the reactivity between PbI_2, the neutral amines, and their cations are different from one another, further supporting our discussion from the energy diagram with respect to the activation energy.

To explore the thermodynamics regarding the n = 2 RP-phases, we used the n = 1 materials formed in the first reaction as the precursors for a second reaction (**Supporting Video 2**). We separately prepared a formamidinium acetate solution (FAOAc) in toluene and butyric acid and swiftly injected it into the n = 1 precursors (see experimental section for details). The introduction of this A-site cation allows the formation of $n \geq 2$ RP-phases. Upon addition of FA^+ cations to the $(PEA)_2PbI_4$ precursor, nothing happens at first; after a few minutes, under 80 °C heat, a slow reaction takes place, and we can see a gradual change of colors from yellow (n = 1 phase) to orange/red (n = 2 phase) until the end of the time-lapse (**Figure S14** shows selected pictures during the reaction). This observation confirms our hypothesis that the formation energy depth for PEA_2PbI_4 is deeper than for its higher phases ($n \geq 2$). For TMA, the addition of FA^+ cations causes an immediate reaction, resulting in a dark-red/brown product (meaning a mixture of $n \geq 2$ phases) at room temperature; this brown product, upon 80 °C heat, slowly changes to bright-red color with time, which means interconversion of higher phases to n = 2 or n = 3 phases. The fact that $(TMA)_2PbI_4$ promptly reacts with FA^+ cations indicates that the n = 1 and higher-order phases have similar formation energy depths

and that the activation energy for this reaction is low ($E_a < k_BT$). **Figure S4** shows the XRD patterns of the products from **Supporting Video 2**. More accurate, quantitative calorimetry will certainly provide more precise conclusions, but this simple, visual experiment is consistent with the observations from **Figure 1** through **Figure 3** and the qualitative mechanisms we propose in the energy diagram of **Figure 4**.

The molecular origin of the different dynamics observed for PEAI and TMAI

We hypothesize that the origin of the different reactivity between PEAI and TMAI is in the steric effects. While the PEA^+ cation has two fully rotational bonds in the alkyl chain: the C-N and C-C; the TMA^+ has only a single rotational bond: the C-N (see **Figure S15**). This higher rotational and vibrational degrees of freedom of the alkyl chains influences their reaction dynamics. For instance, due to their similarity, one could expect that BZA^+ has similar reaction dynamics as the PEA^+. However, the BZA^+ reactivity is very similar to the reactivity of TMA^+. In the reaction conditions of **Supporting Video 1**, both TMA^+ and BZA^+ form a clear yellow solution by dissolving PbI_2, rather than forming the n = 1 RP-phase, as in the case of PEA^+. Also, in the reaction conditions of the **Supporting Video 2**, both form the dark-brown solid that, upon heating, develops to a vivid red solid, suggesting the formation of n = 2 and n = 3 RP-phases. These observations regarding BZA^+ reactions can be verified in the reference [1] of this material. In addition, following a similar reasoning, PEA^+ and TEA^+ show similarities in their reactivity. For instance, in the work of Sutano et al.,[7] the perovskite film treated with an IPA solution of TEAI leads to the formation of mostly n = 1 RP-phases with some evidence of n = 2. This is exactly what we observe for PEA^+; the n = 1 RP-phase remains the predominant phase even after prolonged thermal annealing, in close agreement to what we observe in this work and previous reports.[7,8] Finally, the type of aromatic ring (benzene/thiophene) must also play a role, especially in the effectiveness of the van der Waals interactions in the bilayer of organic cations; however, the steric effects seem to be more important.

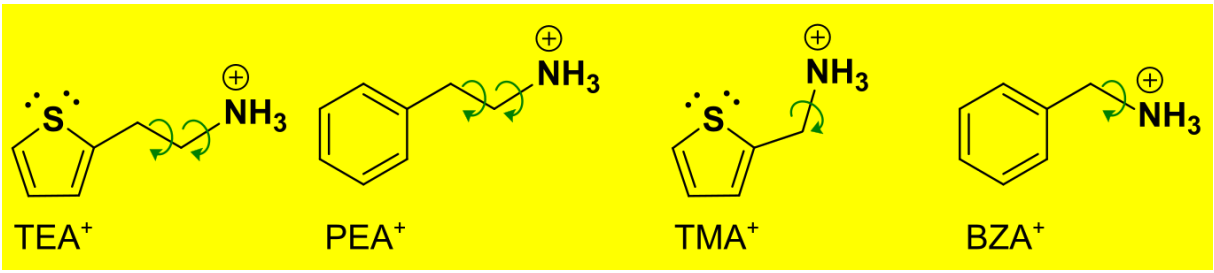

Figure S15. Molecular structure of the cations used in this work (PEA^+ and TMA^+) and their analogs (BZA^+ and TEA^+, respectively).

References

[1] R. F. Moral, L. G. Bonato, J. C. Germino, W. X. Coelho Oliveira, R. Kamat, J. Xu, C. J. Tassone, S. D. Stranks, M. F. Toney, A. F. Nogueira, *Chem. Mater.* **2019**, *31*, 9472.
[2] Q. Du, C. Zhu, Z. Yin, G. Na, C. Cheng, Y. Han, N. Liu, X. Niu, H. Zhou, H. Chen, L. Zhang, S. Jin, Q. Chen, *ACS Nano* **2020**, *14*, 5806.
[3] R. F. Moral, J. C. Germino, L. G. Bonato, D. B. Almeida, E. M. Therézio, T. D. Z. Atvars, S. D. Stranks, R. A. Nome, A. F. Nogueira, *Adv. Opt. Mater.* **2020**, *8*, 2001431.
[4] D. Feldstein, R. Perea-Causín, S. Wang, M. Dyksik, K. Watanabe, T. Taniguchi, P. Plochocka, E. Malic, *J. Phys. Chem. Lett.* **2020**, *11*, 9975.
[5] R. F. Warren, W. Y. Liang, *J. Phys. Condens. Matter* **1993**, *5*, 6407.
[6] C. C. Coleman, H. Goldwhite, W. Tikkanen, *Chem. Mater.* **1998**, *10*, 2794.

[7] A. A. Sutanto, N. Drigo, V. I. E. Queloz, I. Garcia-Benito, A. R. Kirmani, L. J. Richter, P. A. Schouwink, K. Taek Cho, S. Paek, M. Khaja Nazeeruddin, G. Grancini, J. Mater. Chem. A 2020, 8, 2343.
[8] A. A. Sutanto, R. Szostak, N. Drigo, V. I. E. Queloz, P. E. Marchezi, J. C. Germino, H. C. N. Tolentino, M. K. Nazeeruddin, A. F. Nogueira, G. Grancini, Nano Lett. 2020, 20, 3992.